1 **Phase equilibrium experiments and thermodynamic simulations to**

2 **constrain the pre-eruptive conditions of the 2021 Tajogaite eruption**

3 **(Cumbre Vieja volcano, La Palma, Canary Islands)**

4

5 Alessandro Fabbrizio[a,*], Emily C. Bamber[b], Eleni Michailidou[a], Jorge E.

6 Romero[c,d], Fabio Arzilli[e], Barbara Bonechi[d], Margherita Polacci[d], Mike

7 Burton[d]

8

9 [a]*Institute of Petrology and Structural Geology, Faculty of Science,*

10 *Charles University, Albertov 6, 128 43 Prague, Czech Republic*

11

12 [b]*Department of Earth Sciences, University of Turin, Via Valperga*

13 *Caluso, 35, 10125, Turin, Italy*

14

15 [c]*Instituto de Ciencias de la Ingeniería, Universidad de O'Higgins,*

16 *Libertador Bernardo O'Higgins 611, Rancagua, Chile*

17

18 [d]*Department of Earth and Environmental Sciences, The University of*

19 *Manchester, Manchester M13 9PL, United Kingdom*

20

21 [e]*School of Science and Technology, Geology Division, University of*

22 *Camerino, Camerino, Italy*

23

24 [*]Corresponding author.

25 *Email addres*s: alessandro.fabbrizio@natur.cuni.cz (A. Fabbrizio).

Abstract

Phase relations of a tephritic lava erupted at La Palma, Canary Islands, the 2nd of October 2021, during the eruption of Cumbre Vieja volcano were determined experimentally in the temperature/water content space, T (°C)/H_2O (wt%). The crystallisation experiments were carried out at a fixed pressure of 275 MPa for temperatures varying from 1000 to 1200 °C and with H_2O added contents ranging from 0 to 5 wt%. Results from the synthetic products are compared with those obtained from thermodynamic simulations and with the natural phases to constrain the pre-eruptive conditions of the tephritic magma stored in the shallow reservoir. The major phases (clinopyroxene + olivine + oxides) occurring in the natural products were reproduced. The experimental results combined with thermodynamic modelling allow us to constrain the pre-eruptive temperature to ~1100 °C considering H_2O to 3 wt% and to restrict the crystallisation of plagioclase at low pressures (< 20 MPa). The results indicate that, under the presence of a pure H_2O fluid, amphibole is stable at pressures higher than 300 MPa and temperatures ~1000 °C. Our results on pre-eruptive conditions of the 2021 Tajogaite eruption provide important constraints on mechanisms of storage and transport in primitive alkaline magmas.

1. Introduction

This experimental study focuses on the physical parametrization of the recent eruption which happened in La Palma, one of the most historically active volcanic islands of the Canarian Archipelago. Particularly, we aim to constrain the pre-eruptive conditions of the 2021 Cumbre Vieja eruption (Tajogaite volcano, La Palma, Canary Islands) that began on 19 September 2021 after 40 years of quiescence and ended on 13 December 2021. Seismicity during the eruption indicates magma intrusions at 8-12 and 20-25 km depth (D'Auria et al., 2022). The erupted rocks are tephritic-basanitic in composition (Carracedo et al., 2022; Castro and Feisel, 2022; Day et al., 2022; Dayton et al., 2023; Di Fiore et al., 2023; Pankhurst et al., 2022; Romero et al., 2022; Ubide et al., 2023). Over the course of three months, the Tajogaite volcano displayed hybrid volcanic activity consisting of effusive phases with emission of lava flows, explosive phases with pyroclastic columns reaching 8500 m asl (PEVOLCA, 2021), with resulting ash-falls spread all over La Palma, and intense degassing from different simultaneously active craters (Bonadonna et al., 2022; Martínez-Martínez et al., 2023).

Previous works have examined magma migration from the mantle to the surface, the pressure-temperature conditions that produced exceptionally fast and fluid lava at high discharge rates, the eruptive dynamics and cone collapse, the depths of magma storage, the geochemical variations over the entire eruptive period, and the effects of the eruption on La Palma infrastructure and inhabitants (Bonadonna et

76   al., 2022; Carracedo et al., 2022; Castro and Feisel, 2022; Day et al.,

77   2022; Dayton et al., 2023; Padron et al., 2022; Romero et al., 2022; Di

78   Fiore et al., 2023; Ubide et al., 2023). However, an experimental

79   constraint of the pre-eruptive conditions within the Cumbre Vieja

80   plumbing system is still lacking.

81   In this study, phase equilibria for tephritic magma were

82   determined at fixed pressure in the T-H_2O wt% space by laboratory

83   experiments and thermodynamic modelling to define the pre-eruptive

84   conditions of the 2021 Cumbre Vieja eruption.

85   The Canary Islands represent, after Hawaii, the most important

86   example of hot spot related volcanism (Cas et al., 2022) and its

87   volcanoes are among the most active on Earth, as shown by the recent

88   eruptions of El Hierro (2011-2012) and Cumbre Vieja (2021).

89   Mantle plume-related magmatism (hot spot zones) in

90   intracontinental settings and oceanic environments may produce either

91   short-lived voluminous eruptions of basaltic magmas or build an oceanic

92   island volcano (e.g. Houghton and Gonnermann, 2008; Caracciolo et al.,

93   2021; Cas et al., 2022). Mantle plumes can produce a relatively large

94   amount of magma, which can migrate from the mantle to the surface.

95   The pressure and temperature conditions controlling magma storage

96   within the crust and magma eruptability in plume-related volcanism

97   have been investigated in previous studies (e.g. Klugel et al., 2005;

98   Haddadi et al., 2017; Oglialoro et al., 2017; Padron et al., 2022), where

99   the pre- and syn-eruptive conditions were constrained by mineral-melt

100   thermobarometry, melt and fluid inclusions (e.g. Hildner et al., 2012;

101   Bali et al., 2018; Hartley et al., 2018). However, phase equilibrium

102   studies to constrain the pre-eruptive conditions of this style of volcanism

103   are still scarce (Martí et al., 2013).

104   Previous phase equilibrium studies which determined the pre-

105   eruptive conditions for a series of eruptions of the Canary Islands

106   include: Abrigo 190 kyr ago (Andújar et al., 2008); Montaña Blanca

107   2020 y.b.p. (Fabbrizio et al., 2006; Andújar and Scaillet, 2012); Teide-

108   Pico Viejo 1800 y.b.p. (Andújar et al., 2013); Teide 1150 y.b.p.

109   (Andújar et al., 2010), El Hierro 2011-2012 (Martí et al., 2013). All

110   these studies, with the exception of Martí et al. (2013), investigated

111   phase equilibria for phonolitic compositions, constraining the pre-

112   eruptive storage of magma at relatively shallow depths ($\leq$ 150 MPa) and

113   temperatures lower than 900 °C. Martí et al. (2013) performed a phase

114   equilibrium study, combined with mineral-melt geothermometry and

115   thermodynamic modelling, for basanitic compositions at a fixed

116   pressure of 400 MPa, constraining the pre-eruptive temperature in the

117   range of 1100-1185 °C.

118   Given magma reservoirs are inaccessible, the synthetic

119   reproduction of natural phase compositions and assemblages using

120   crystallisation experiments allows us to constrain intensive parameters

121   such as temperature, pressure, oxygen fugacity and volatile content.

122   Therefore, we can characterize the conditions of magmas before

123   eruptions. Equilibrium experiments are also used to obtain phase

124   diagrams in which mineral phases' stability fields are constrained as a

125   function of pressure (P), temperature (T) conditions, water content (H_2O

126 wt%) and/or mixed fluid (XH$_2$O). Therefore, equilibrium crystallisation

127 experiments help to reproduce the mineral assemblage, chemical

128 compositions of the phases and textures of erupted products. The

129 comparison between the chemistry and the texture of the run products

130 with those of the natural samples allows the pre-eruptive conditions of

131 the volcanic system to be defined. This kind of study is critical in order

132 to better understand the behavior of explosive eruptions given the

133 profound economic and societal consequences such eruptions can

134 produce (Blundy and Cashman, 2008). Moreover, experimental

135 petrology data for understudied magmatic systems are pivotal to

136 improve the accuracy of mineral-melt thermobarometry. In turn, the

137 experimentally derived pre-eruptive conditions can help risk-managers

138 and decision-makers improve volcano monitoring and disaster

139 mitigation systems.

140

141 **2. Experimental and analytical methods**

142

143 *2.1. Strategy*

144

145   We performed equilibrium crystallisation experiments using

146 tephritic compositions, which represent the most common compositions

147 erupted during the first three weeks of the 2021 Cumbre Vieja eruption

148 (Day et al., 2022). Most of the reported experiments were performed

149 under hydrous conditions with 1, 3 and 5 wt% H$_2$O added. The

150 experiments were run with different water contents to test the stability

151 fields of the mineral phases. The experimental pressure was fixed to 275

152 MPa to simulate equilibrium crystallisation in the shallow magmatic

153 reservoir located at a depth of 8-12 km (D'Auria et al., 2022).

154

155 *2.2. Starting materials*

156

157 The tephritic natural starting material (CVLP-LF3, Table 1) was

158 erupted on 2 October 2021 and collected the day after during a field

159 campaign carried out between 20 September and 20 October 2021

160 (Romero et al., 2022), hence representing some of the products erupted

161 in the initial phase of the event. The sample is glassy, highly vesiculated

162 and contains phenocrysts of clinopyroxene, Fe-Ti oxides, olivine and

163 plagioclase microlites. Using this sample, one anhydrous and two

164 hydrous (with 1 and 3 wt% H_2O added) starting materials were prepared.

165 The anhydrous starting material was created by grinding, in an

166 agate mortar under ethanol, a few grams of the tephrite (CVLP-LF3;

167 Romero et al., 2022) into a fine homogenous powder. A hydrous-rich (5

168 wt% H_2O added, Table 1) starting material, representing a synthetic

169 mixture analogue to the composition of the natural tephrite, was

170 obtained by mixing a total of 1 g of oxides (SiO_2, TiO_2, Al_2O_3, FeO,

171 MgO, MnO), hydroxides ($Al(OH)_3$), silicates ($CaSiO_3$, Na_2SiO_3,

172 K_2SiO_3) and phosphate ($Ca_5(OH)(PO_4)_3$) in appropriate proportions. All

173 chemical compounds were new and when opened were stored at 110 °C

174 prior to weighing and mixing. All powders were homogenized in an

175 agate mortar under ethanol. A suite of trace elements (Li, Rb, Cs, Co,

176 Cu, Zn, Sr, Cd, Ba, Pb, Sc, Cr, Ga, Y, La, Ce, Pr, Nd, Sm, Eu, Gd, Tb,

177 Dy, Ho, Er, Tm, Yb, Lu, Ge, Zr, Sn, Hf) were added to the anhydrous

178 and to the hydrous-rich starting mixtures as oxides or chlorides in an

179 amount totalling 1 wt%, resulting in individual trace elements

180 concentrations of ~200 to 300 ppm. These mixtures were re-ground

181 under ethanol after each addition.

182 The other hydrous starting materials (1 and 3 wt% H_2O added)

183 were created by mixing in appropriate amounts, in an agate mortar

184 under ethanol, the natural anhydrous composition with the hydrous-rich

185 synthetic analogue. All prepared starting materials (Table 1) were stored,

186 prior to their encapsulation, in a furnace at 110 °C to prevent water and

187 CO_2 adsorption.

188

189 *2.3. Quickpress experiments*

190

191 The experiments (Table 2) were carried out at the Experimental

192 Petrology Laboratory of the Institute of Petrology and Structural

193 Geology (Charles University) in a Quickpress non-endloaded piston

194 cylinder apparatus at 275 MPa in the temperature range 1000 to 1200 °C.

195 Approximately 20 mg of the starting powders were loaded into

196 cylindrical $Au_{80}Pd_{20}$-capsules (OD: 3 mm, ID: 2.7 mm). Capsules were

197 sealed by arc-welding under a flux of argon that cooled them. The

198 employed 19-25 mm NaCl-pyrex-graphite-MgO low-pressure

199 assemblies impose relatively oxidizing conditions at about 2-log units

200 above the Ni-NiO buffer (Masotta et al., 2012). Temperature was

201   measured by factory-calibrated S-type ($Pt-Pt_{90}Rh_{10}$) thermocouples with

202   an accuracy of ± 2 °C. Runs were cold-pressurized to a pressure 10%

203   higher than the target value, then the pressure was decreased down to

204   275 MPa. No correction was applied for the pressure effects on e.m.f.

205   Experiments were first heated at a rate of 15 °C/min to 700 °C to allow

206   a gently dissociation of $Al(OH)_3$, then raised to 1200 °C (superliquidus)

207   with a rate of 50 °C/min. The superliquidus temperature was maintained

208   for 1 hour to allow melt homogenization and then decreased to the target

209   temperature at a cooling rate of 60 °C/h. Run duration at the final

210   temperature $\geq$ 1100 °C was 24 hours and 48 hours below 1100 °C. One

211   reversal experiment, here the term reversal is used to indicate runs that

212   were performed with a different thermal/temporal history compared to

213   the one described above, was performed by keeping it at 1100 °C for 48

214   hours after cooling from superliquidus temperature. A second reversal

215   experiment was performed by heating the assembly directly from room

216   temperature to 1100 °C and keeping the temperature constant for 24

217   hours. The advantage of heating the experimental charge at

218   superliquidus temperature and then cooling it at target temperature is

219   that resting at superliquidus temperature promotes chemical

220   homogeneity of the melt (by melting of all residual crystal nuclei in the

221   case of a natural-rock powder or by complete reaction of the chemical

222   compounds in the case of a synthetic starting material) from which few

223   and large crystals will precipitate once the run is at target temperature.

224   On the other hand, the direct heating of the experimental charge from

225   room to target temperature does not guarantee reaching chemical

226 homogeneity before crystallisation begins because of the presence of

227 residual crystal nuclei or incomplete reaction of the chemical

228 compounds. Moreover, experimental charges heated directly to final

229 temperature will be characterized by a large number of crystals with

230 small size (nucleation enhanced versus growth) compared to the textures

231 obtained from the experiments cooled from superliquidus temperature

232 (growth enhanced versus nucleation). Consequently, a good agreement

233 between the mineralogical assemblage and the chemistry of the phases

234 obtained in runs performed with these different strategies can be

235 considered as a proof that equilibrium, or at least near-equilibrium,

236 conditions were attained. All experiments were terminated by switching

237 off the power, resulting in a cooling rate >100 °C/s. Pressure was kept

238 constant during quench. The recovered capsules were mounted in epoxy

239 and polished for analysis.

240

241 *2.4. Analytical techniques*

242

243 Back-scattered electron images (BSE) of the samples and the

244 major and minor component concentrations of run products were

245 obtained using the JEOL JXA-8530F Electron Microprobe Analyzer

246 (EMPA) at the Institute of Petrology and Structural Geology, Charles

247 University. Analytical conditions for mineral phases were 15 kV, 10 nA

248 beam current, 1 μm beam size and counting times of 20 s for all

249 elements with half-time on background. Glasses were analyzed under

250 the same conditions with the exception of the beam size that was set to

251 10 µm. Alkalis (Na, K) were analyzed first in order to minimize their

252 loss during glass analyses. Measurement errors based on counting

253 statistics were <10% for all elements in all phases. The following

254 standards were used for calibration: quartz (Si), corundum (Al), rutile

255 (Ti), chromium oxide (Cr), vanadinite (V), magnetite (Fe), periclase

256 (Mg), rhodonite (Mn), calcite (Ca), albite (Na), sanidine (K), apatite (P),

257 topaz (F), halite (Cl). The ZAF correction was used to perform the data

258 reduction. The analyses for minerals and glasses as well as BSE images

259 of the experimental charges are presented in Supplementary Table 1.

260

261 **3. Results**

262

263 *3.1. Phase equilibria*

264

265 BSE images of all experiments are shown in Supplementary

266 Table 1 and a selection of them is shown in Fig. 1. Experimental results

267 are reported in Table 2. The attainment of equilibrium is indicated by

268 the homogenous distribution of phases in all experimental charges and

269 the run duration (24 h at 1100-1200 °C; 48 h at 1000-1050 °C), which is

270 similar to those of previous phase equilibrium studies on basaltic

271 systems (e.g., Arzilli et al., 2015; La Spina et al., 2016; Polacci et al.,

272 2018). As a comparison, one day at 1060 °C/1 atm was found to be

273 sufficient for an andesite to reach a steady state with respect to the melt

274 composition and phase assemblage (Baker and Eggler, 1987).

275 Additional evidence which indicates the attainment of equilibrium in the

276   experiments includes the euhedral shapes of mineral phases and the

277   close correspondence in both texture and composition between the three

278   experiments performed at 1100 °C/1 wt% H_2O with different temporal

279   and thermal strategies (i.e., resting at 1100 °C for 24 and 48 h after

280   cooling from 1200 °C; direct heating to 1100 °C and resting for 24 h).

281   The experimental results (Fig. 2) highlight that with up to 1 wt%

282   water added, olivine crystallises between 1150 and 1175 °C, followed

283   by clinopyroxene between 1100 and 1125 °C. With increasing water

284   content, the appearance of olivine is lowered to 1100-1125 °C (3 wt%

285   H_2O) and <1000 °C (5 wt% H_2O). Instead, the appearance of

286   clinopyroxene is not affected by the water content (0-5 wt% H_2O),

287   which is always in the temperature interval 1100-1125 °C. The

288   crystallisation temperatures of oxides (Cr-spinel and Ti-magnetite) are

289   strongly influenced by the water content, decreasing for Cr-spinel from

290   ~1200 °C at anhydrous conditions to ~1125 °C with 3 wt% water added

291   and for Ti-magnetite decreasing from ~1100 to ~1000 °C, respectively,

292   with 5 and 1 wt% H_2O added. Amphibole and apatite were only found at

293   1000 °C/1 wt% H_2O.

294

295   *3.2. Description of the experimental charges*

296

297   The experimental runs (1 wt% H_2O) performed at temperatures

298   equal to or higher than 1175 °C are superliquidus, as well as those with

299   3 and 5 wt% H_2O added at temperatures of 1150 °C and equal or higher

300   than 1125 °C, respectively (Supplementary Table 1; Fig. 2). The first

301   phase to appear is oxide, as Cr-spinel (Cr-sp; 0 wt % H_2O/1175 °C, 1

302   wt% H_2O/1150 °C, 3 wt% H_2O/1125 °C) or Ti-magnetite (Ti-mt; 5 wt%

303   H_2O/1150 °C). Oxides are mostly euhedral, with sizes between 5-10 μm

304   for Cr-spinel and 30-40 μm for Ti-magnetite (Fig. 1; Supplementary

305   Table 1). Cr-spinel and Ti-magnetite never coexist in the same

306   experimental charge (see section 4.1 for a detailed explanation).

307   Olivine is present in the experimental charges with up to 3 wt%

308   H_2O added. The shape of olivine crystals changes as a function of the

309   degree of undercooling (i.e., ΔT, the temperature difference between the

310   liquidus temperature of the specific mineral phase and its crystallisation

311   temperature; Kirkpatrick, 1981), as already observed in previous

312   experimental studies (Faure et al., 2003; Faure et al., 2007; Lang et al.,

313   2021). In experimental runs performed at a low degree of undercooling

314   (i.e., ΔT= ~12 °C, runs at 0 wt% H_2O/1150 °C, 1 wt% H_2O/1150 °C, 3

315   wt% H_2O/1100 °C), olivine is euhedral, with a size ranging from 30 to

316   100 μm. At higher degrees of undercooling (ΔT= ~37 °C) and a

317   temperature of 1125 °C, olivine crystals are mostly euhedral with some

318   crystals hosting a melt pocket (0 wt% H_2O/1125 °C). As the degree of

319   undercooling increases (ΔT= ~62 °C) in the runs performed at 1100 °C

320   with up to 1 wt% H_2O added, olivine crystals are mostly skeletal with

321   embayments, hosting one or multiple melt pockets, although rare

322   euhedral crystals are still present (Fig. 1; Supplementary Table 1). The

323   reversal run performed at 1100 °C for 48 h after cooling from 1200 °C is

324   characterized by olivine crystals that are mostly euhedral (some hosting

325   a melt pocket). The run heated directly to 1100 °C shows only euhedral

326 olivine crystals, suggesting that the skeletal shapes are a direct

327 consequence of the degree of undercooling and of the experimental time

328 spent at the final temperature. At the lowest temperature, i.e.,

329 1000 °C/highest degree of undercooling (ΔT= ~162 °C), olivine crystals

330 show only skeletal shapes (Shea et al., 2019).

331   Clinopyroxene appears in all runs performed at or below

332 1100 °C. At 1100 °C crystals are euhedral with zones enriched in Si-Mg

333 (darker areas in the BSE images) and in Ti-Al (brighter areas in the BSE

334 images) and with sizes exceeding 100 μm, occasionally hosting a melt

335 pocket (Fig. 1; Supplementary Table 1). The different zones enriched in

336 Si-Mg and Ti-Al have already been observed in clinopyroxene crystals

337 crystallising from undercooled melts (Colle et al., 2023; Masotta et al.,

338 2020; Moschini et al., 2021; MacDonald et al., 2022). In the runs

339 performed at 1000 and 1050 °C clinopyroxene crystals are mostly

340 euhedral, and they host multiple melt pockets or they are characterized

341 by the presence of embayments (Supplementary Table 1). Rare euhedral

342 crystals of amphibole (15-30 μm wide) and apatite (<15 μm wide)

343 crystallised in the run performed at 1000 °C with 1 wt% H_2O added

344 (Supplementary Table 1).

345

346 *3.3. Phase compositions*

347

348   The chemical compositions of the residual glasses

349 (representative of the residual melt compositions produced by

350 crystallisation, Fig. 3), clinopyroxene, olivine, Cr-spinel, Ti-magnetite,

351   apatite, and amphibole are reported in Supplementary Table 1. The

352   compositions of the residual melts change according to the phase

353   equilibria. The apparent low total of the anhydrous glasses (95-97 wt%)

354   are due either to trace elements (1 wt%) not measured during analysis

355   and to their increased concentration (>1 wt%) in the residual melts with

356   progressing crystallisation, either to small or negligible hygroscopic

357   water absorption during capsule preparation or hydrogen diffusion into

358   the capsule during the run (Fabbrizio et al., 2021), or either to element

359   migration and redox changes caused by sub-surface charging effects

360   during analysis (1 wt%; Hughes et al., 2019). The combination of these

361   effects suggest negligible or no water contamination of the anhydrous

362   glasses. The SiO_2 contents start to increase noticeably with the initiation

363   of clinopyroxene crystallisation between 1100 and 1125 °C. The trend

364   in Al_2O_3 content as a function of temperature is also similar to that of

365   SiO_2. In correspondence with the onset of clinopyroxene crystallisation,

366   CaO contents start to decrease with its appearance below 1125 °C.

367   Considering all the experiments performed in this study, the MgO

368   content of residual glasses decreases as a result of oxides, olivine and

369   clinopyroxene crystallisation. The compositions of residual glasses

370   indicate that FeO trends are not affected by Cr-spinel and olivine

371   crystallisation, as their FeO concentrations tend to decrease markedly

372   only after the appearance of clinopyroxene and of Ti-magnetite. The low

373   FeO content in the residual glass at 1125 °C with 5 wt% H_2O may

374   suggest some iron loss during this run. TiO_2 can be considered roughly

375   constant in all glasses given that it decreases markedly only after the

376 appearance of Ti-magnetite. MnO contents tend to increase with

377 decreasing temperature, reach a maximum at 1100 °C and then decrease

378 abruptly at lower temperature with the appearance of Ti-magnetite.

379 Alkalis (i.e., Na_2O and K_2O) increase markedly with the appearance of

380 clinopyroxene. P_2O_5 contents increase steadily with the appearance of

381 clinopyroxene, the crystallisation of apatite at 1000 °C in the run with 1

382 wt% H_2O buffers its increase.

383 The forsterite contents of experimental olivine vary between

384 Fo_{82} and Fo_{87} as a function of the experimental temperature (Fig. 4).

385 Clinopyroxene in the experimental charges shows a fairly constant

386 diopsidic composition with temperature, ranging from $Wo_{46}En_{47}Fs_8$ to

387 $Wo_{52}En_{32}Fs_{16}$ (Fig. 4). Oxides (Cr-spinel) and apatite were difficult to

388 analyze due to their small size, but analyses free of contamination from

389 other phases are reported in Supplementary Table 1. Ti-rich kaersetutic

390 (6 wt% TiO_2) amphibole (Supplementary Table 1) only crystallised at

391 1000 °C in the charge with 1 wt% H_2O added.

392

393 **4. Discussion**

394

395 In the following sections we will compare the experimental

396 results with the natural erupted products and with crystallisation

397 simulations performed by MELTS. We will use the experimental and

398 thermodynamic results to infer the pre-eruptive temperature and water

399 contents of the magma stored in the shallow reservoir at a corresponding

400 pressure of 275 MPa (D'Auria et al., 2022).

401 *4.1. Comparison with the natural erupted rocks*

402

403   Comparing the experimental results with the natural lava and

404 tephra (Castro and Feisel 2022; Day et al., 2022; Pankhurst et al., 2022;

405 Romero et al., 2022) we observe that the natural phase assemblage of

406 clinopyroxene, olivine and oxides is well reproduced in terms of mineral

407 phase composition and texture by the experiments performed at 1100 °C

408 with up to 3 wt% H_2O added. This water content is comparable with

409 previous estimations of H_2O content for historical erupted products of

410 Cumbre Vieja (Weis et al., 2015) and for oceanic island basalts

411 (Kovalenko et al., 2007) as well as with the melt H_2O content (0.8 wt%,

412 plagioclase-liquid hygrometer) determined by pairs of plagioclase

413 microlites and matrix glass for the erupted tephra of the 2021 eruption

414 of Cumbre Vieja (Castro and Feisel 2022). The above water content is

415 also in agreement with the melt water contents estimated for undegassed

416 Canary magmas (Longpré et al., 2017; Walowski et al., 2017; Taracsak

417 et al., 2019).

418   Experimental clinopyroxene (Figs. 4, 5), is the most abundant

419 phase, with euhedral crystals characterized by sector zoning, the

420 observed compositions are in a quite narrow range from $Wo_{46}En_{47}Fs_8$ to

421 $Wo_{52}En_{32}Fs_{16}$, reproducing well the clinopyroxene compositions (Wo_{47}

422 $En_{40}Fs_{13}$-$Wo_{51}En_{33}Fs_{16}$) of the natural tephra and lava (Castro and Feisel

423 2022; Day et al., 2022; Pankhurst et al., 2022; Romero et al., 2022).

424   The experimental olivine (Fig. 4) compositions range from Fo_{82}

425 to Fo_{87}, comparable to those of natural olivine crystals (Fo_{78}-Fo_{86}) as

426 well as skeletal and rounded-embayed shapes similar to those observed

427 in the natural samples (Day et al., 2022; Pankhurst et al., 2022; Dayton

428 et al., 2023).

429 The presence of Ti-magnetite in the runs with 5 wt% H_2O added

430 as well as in the high-crystalline run performed at 1000 °C/1 wt% H_2O

431 coupled with the absence of Cr-spinel in the runs performed at higher

432 water contents suggests that oxide stability is influenced by the degree

433 of evolution of the residual melt from where it precipitates. Ti-magnetite

434 is associated with more evolved melts whereas Cr-spinel crystallises in

435 more primitive melts. This experimental evidence is corroborated by the

436 observation that Ti-magnetite is found in the earliest and more evolved

437 erupted lavas, which have compositions that extend to phonotephrite

438 (Day et al., 2022). Moreover, the less evolved erupted lavas have higher

439 Cr_2O_3 contents than the more evolved ones, thus favoring the

440 crystallisation of Cr-spinel (Day et al., 2022).

441 Hydrous phases such as amphibole and apatite are present only

442 in the run at 1000 °C/1 wt% H_2O suggesting that their crystallisation

443 was related to a relative increase of the water content in the residual

444 melt due to the high crystallinity of this experimental charge. The

445 natural products erupted between 19-27 September show kaersutitic

446 amphibole crystals with evident reaction rims (Day et al., 2022;

447 Pankhurst et al., 2022; Romero et al., 2022; Ubide et al., 2023)

448 suggesting that amphibole was outside of its stability field during the

449 ascent and storage of magma at a shallow depth within the crust. The

450 lack of amphibole crystals in the experimental charges could imply that

451 amphibole crystallised from a hotter and more primitive magma at

452 pressures higher than 275 MPa. However, the more primitive products

453 erupted after 27 September are amphibole-free (Ubide et al., 2023)

454 ruling out the above reasoning. Since we used a composition erupted on

455 the 2nd of October (i.e., amphibole-free) the lack of amphibole crystals

456 in the experimental charges is in agreement with the observation of the

457 amphibole-free erupted samples and its presence in the more evolved

458 magmas should be related to other parameters rather than to the effect of

459 the pressure. Phase relations of alkaline and tholeiitic basalts (Freise et

460 al., 2009; Iacovino et al., 2016) show that the presence of a mixed H_2O-

461 CO_2 fluid has the effect to increase up to ~50 °C the thermal stability of

462 amphibole compared to its appearance in a system with a pure H_2O fluid.

463 Recent crystallisation experiments performed under variable H_2O/CO_2

464 ratios for compositions erupted during the Tajogaite 2021 eruption point

465 out that amphibole is stable up to 1065 °C (Andújar et al., 2023). We

466 note that by expanding the stability field of amphibole by 50 °C (Fig. 2)

467 we would be close to the maximum crystallisation temperature

468 experimentally reproduced by Andújar (2023). Following this

469 experimental evidence and these considerations we suggest that

470 amphibole might have crystallised in the shallow reservoir at 275 MPa

471 in the presence of a mixed H_2O-CO_2 fluid and that its reaction rims

472 might have recorded its destabilization during the ascent of the magma

473 towards the surface.

474   The absence of plagioclase in the experimental runs is in

475 agreement with observations of natural samples, where it is present as a

476   microcryst phase in the matrix (Castro and Feisel 2022; Day et al., 2022;

477   Pankhurst et al., 2022; Romero et al., 2022), suggesting that plagioclase

478   nucleated and grew during magma ascent in the volcanic conduit and/or

479   during cooling of the lava outside the vent. In general, the textures and

480   chemical compositions observed in the experimental charges are in good

481   agreement with those of the natural samples.

482   Regarding the residual glass (Fig. 3), we note that the SiO_2

483   contents of the anhydrous experimental glasses and of those with 1 and

484   3 wt% H_2O added match the SiO_2 contents of the natural glasses at

485   temperatures between 1100 and 1125 °C. For the same range of

486   temperature, the experimental glasses with up 1 wt% H_2O added have

487   Al_2O_3 contents which correspond to natural glass compositions. All

488   experimental melts obtained at 1100 °C or at a higher temperature

489   replicate the CaO contents of the natural glasses. The best match for the

490   MgO content of natural glasses is found within the range 1035-1125 ˚C

491   and 1000-1114 °C, respectively, for charges with 1 and 5 % H_2O added.

492   The FeO content of the natural glasses is well reproduced in the

493   experiments performed at 1100-1125 °C. The TiO_2 concentrations of

494   natural glasses are in good agreement with glasses produced in

495   experiments at temperatures above 1050 °C, independent of the water

496   content. With the exception of the experimental glasses obtained with 5

497   wt% H_2O, all other glasses have MnO contents encompassing the

498   natural glass composition. The alkali contents of the natural glasses

499   show the best correspondence with experiments with up to 1 wt% H_2O.

500   The experimental glasses obtained at 1100 °C with up to 1 wt% H_2O

501   have P_2O_5 contents with the closest resemblance to natural compositions.

502

503   *4.2. Comparison with Rhyolite-MELTS modelling*

504

505   In this section the experimental results are compared with those

506   obtained by using the software package Rhyolite-MELTS designed for

507   thermodynamic modelling of phase equilibria in magmatic systems

508   (Ghiorso and Sack, 1995; Gualda et al., 2012). The thermodynamic

509   modelling was performed for the same tephritic composition (CVLP-

510   LF3 of Romero et al., 2022) used as the experimental starting material

511   and for a slightly less evolved basanite (Castro and Feisel, 2022) erupted

512   in November during the 2021 Cumbre Vieja eruption. To perform

513   simulations which include the experimental conditions and also expand

514   the T-H_2O-fO_2 space, simulations were performed for both compositions

515   between 900-1300 °C and 0.1 and 800 MPa, for water contents of 0, 1, 3

516   and 5 wt% and at fO_2 values corresponding to the Nickel-Nickel Oxide

517   (NNO) buffer -0.7 and +1.5. The oxygen fugacities in the natural system,

518   estimated by the V-in-olivine oxybarometry technique (e.g. Wang et al.,

519   2019), were calculated to be between NNO + 0.6 and NNO + 1.3 (Day

520   et al., 2022).

521   For all simulations, spinel crystallisation was suppressed. In the

522   parameter space investigated, the inclusion of spinel as a crystallising

523   phase had a significant impact on the crystallisation of olivine. For the

524   tephritic composition, Sp-bearing simulations resulted in solutions

525   where olivine was not found at any condition in the investigated *P-T*-

526   H_2O space for a fO_2 of NNO + 1.5 and only at <10 MPa for a fO_2

527   equivalent to the QFM buffer (i.e., Quartz-Fayalite-Magnetite buffer

528   equivalent to NNO – 0.7). As the experimental results at 275 MPa, fO_2 =

529   NNO + 2 and H_2O = 0-5 wt.% demonstrate that olivine is present as a

530   crystallising phase (Fig. 2), it is possible that the Rhyolite-MELTS

531   underestimates olivine crystallisation when spinel is allowed to

532   crystallise within the investigated parameter space. Instead, when spinel

533   crystallisation is suppressed, olivine is found throughout the *P-T*-H_2O

534   space. For the basanite composition, the suppression of spinel

535   crystallisation results in a 100-150 ˚C increase in the olivine liquidus

536   temperature, depending on the H_2O content. As the basanite

537   composition is comparable to the tephrite, we can suggest from the

538   results of our experiments that the Rhyolite-MELTS simulations could

539   also underestimate the crystallisation temperature of olivine when spinel

540   is allowed to crystallise. As olivine is also present as a phenocryst phase

541   in the natural phase assemblage (Romero et al., 2022; Castro and Feisel,

542   2022; Day et al., 2022), with the crystal content increasing to 10 vol.%

543   during later stages of the eruption (Day et al., 2022), it is important to

544   investigate also the *P-T*-H_2O space of olivine crystallisation using the

545   simulations. Therefore, for our thermodynamic modelling, we chose to

546   exclude spinel crystallisation. For clarity, the results of Rhyolite-

547   MELTS modelling allowing spinel crystallisation are also presented in

548   Supplementary Figures 1 and 2 for comparison.

549　　　　　Anhydrous and hydrous simulations with 1 wt% H_2O performed

550　　for the tephritic composition (Fig. 6) show the crystallisation sequence

551　　clinopyroxene, olivine and plagioclase irrespective of the fO_2 conditions.

552　　Those simulations with 3 wt% H_2O show the appearance of amphibole

553　　only at reduced conditions for pressures higher than 300 MPa and

554　　temperatures lower than 960 °C. By increasing the H_2O content to 5

555　　wt% the stability field of amphibole is enlarged to include pressures

556　　higher than 200 MPa and temperatures lower than 1000 °C for reducing

557　　conditions and pressures higher than 400 MPa and temperatures lower

558　　than 950 °C for oxidizing conditions. Increasing the H_2O content from 0

559　　to 5 wt% also shifts the liquidus temperature of clinopyroxene and

560　　olivine to lower temperatures by 50-60 °C. The stability field of

561　　plagioclase is dramatically reduced to low pressure (<30 MPa) and low

562　　temperature (<1000 ˚C) for H_2O contents of 3 and 5 wt.%. Instead,

563　　plagioclase is found at higher pressure for $H_2O \leq 1$ wt.%, but still at

564　　temperatures <1000 ˚C. Oxidizing conditions tend to slightly increase

565　　the liquidus temperature of clinopyroxene and to decrease that of olivine.

566　　　　　At a corresponding pressure of 275 MPa the crystallisation

567　　temperatures of clinopyroxene predicted by Rhyolite-MELTS are up to

568　　100 °C higher than those observed in the experiments (between 1100

569　　and 1125 °C). The composition of modelled olivine (at 275 MPa) ranges

570　　between Fo_{79-82}, with an increase in Fo as H_2O content increases from 0

571　　to 5 wt.%. For a fixed H_2O content, the Fo content decreases as

572　　temperature decreases from the saturation temperature to 1000 ˚C. For

573　　clinopyroxene, the modelled compositions range between $Wo_{47}En_{46}Fs_8$

574 and $Wo_{39}En_{20}Fs_{41}$, with an enrichment in the Fs component as H_2O

575 content increases. For H_2O contents between 0-1 wt.%, there is a

576 general decrease in the Wo and En components as temperature

577 decreases and a concurrent increase in Fs. However, at higher H_2O

578 contents (3-5 wt.%), Wo and En instead increase and Fs decreases

579 between the liquidus temperature and 1000 ˚C.

580 Modelled melt compositions (Supplementary Figures 3) show

581 comparable trends to the experimental results (Fig. 3), with an increase

582 in SiO_2 and alkalis and a decrease in CaO, MgO and TiO_2 with

583 decreasing temperature. The range in modelled melt chemistry for

584 simulations >1150 ˚C shows good agreement with the range in glass

585 chemistry observed in natural samples. An exception is the FeO trend,

586 where the small decrease in FeO as temperature decreases when

587 compared to the experiments is likely due to suppression of spinel

588 crystallisation in the simulations. Although there is a discrepancy with

589 the modelled liquidus temperature of the phases and that observed in the

590 experiments, the modelled phase compositions and compositional trends

591 show good agreement with the compositional range measured from both

592 natural and experimental olivine and clinopyroxene (Figs. 4, 5).

593 Therefore, while we recognize the limitations of the model,

594 particularly regarding the crystallisation of spinel, the general

595 correspondence of the phase assemblage, crystallisation sequence and

596 phase chemistry between the modelled and experimental results and

597 sample observations suggest that our combined results can provide

598 insight into the pre-eruptive condition of the Tajogaite eruption.

599   The less evolved basanitic composition shows model results (Fig.

600   7) that are substantially different from those obtained by using the

601   tephritic composition. For the basanitic composition, the fO_2 conditions

602   have a greater impact on crystallisation, given that at reducing

603   conditions, the liquidus of clinopyroxene crosses that of olivine. This

604   occurs as the liquidus of olivine is predicted to be steeper than that of

605   clinopyroxene, and as there is a relative small difference between their

606   predicted liquidus temperatures, compared to the larger difference

607   predicted by the tephritic model. When the relatively low fO_2 values

608   enlarge the stability field of olivine the clinoyroxene liquidus is crossed.

609   At 275 MPa the crystallisation temperature of olivine predicted by

610   Rhyolite-MELTS with 1 wt% H_2O and reducing conditions is

611   comparable with the temperature of 1170 ˚C observed in the

612   experiments. However, the liquidus temperature of clinopyroxene is

613   overestimated by ~50 °C, compared to the temperature of 1160 °C

614   observed in the experiments. Similar to the simulations performed with

615   the tephritic composition, water has the effect of reducing the

616   plagioclase stability field to low pressure and low temperature

617   conditions and to stabilize the presence of amphibole, although at low

618   temperatures (<1000 °C). Modelled olivine compositions also differ

619   from the results of tephrite, producing a narrow range in Fo (at 275

620   MPa) of Fo_{85-86}. Fo content also decreases with temperature for a fixed

621   H_2O content.

622   Clinopyroxene compositions vary between $Wo_{43}En_{50}Fs_7$ and

623    $Wo_{31}En_{31}Fs_{39}$, showing an enrichment in the En component compared to

624   the tephritic composition. A similar trend in clinopyroxene composition

625   as a function of H_2O and temperature is observed when compared with

626   the results of the tephritic model. Modelled melt compositions for the

627   basanite composition (Supplementary Figure 4) are comparable to those

628   of the tephrite and the experimental results, with similar trends in major

629   element chemistry as a function of temperature. However, the results of

630   the basanite model have melt compositions more comparable with

631   natural glasses, particularly for Na_2O and P_2O_5.

632   The model results show that amphibole crystallisation is

633   predicted at low-temperature/high-pressure conditions (<1000 °C/>300

634   MPa). These conditions were not investigated in the experiments

635   because they are not considered to be representative of the *T-P*

636   conditions of the Tajogaite shallow reservoir.

637   The thermodynamic models also predict crystallisation of

638   plagioclase at low-temperature/low-pressure conditions (e.g., <25

639   MPa/<950 °C for the tephrite at NNO + 1.5 and 1 wt% H_2O; <25

640   MPa/<1100 °C for the basanite at 1 wt% H_2O). The more sodic

641   composition of modelled plagioclase ($An_{19-35}Ab_{59-71}Or_{4-9}$ for the

642   tephritic composition and $An_{22-67}Ab_{31-71}Or_{1-7}$ for the basanite at 1 wt%

643   H_2O) also shows better agreement with the composition of labradoritic

644   microlites than rare anorthitic phenocrysts in the natural samples

645   (Romero et al., 2022). This thermodynamic observation coupled with

646   the absence of plagioclase in the experimental charges and plagioclase

647   phenocrysts in the natural rocks suggest that plagioclase crystallisation

648   was restricted to magma ascent conditions within the volcanic conduit

649   and/or during the cooling of the erupted rocks outside the vent.

650

651   *4.3. Pre-eruptive conditions*

652

653   Comparison between the phase equilibrium results, the

654   thermodynamic simulations and the natural rocks allows us to constrain

655   the temperature and water content of the magma stored in the shallow

656   reservoir of Cumbre Vieja prior to its eruption. According to our results,

657   the coexistence of the assemblage oxides + olivine + clinopyroxene was

658   reproduced at 1100 °C and with H_2O contents up to 3 wt%. The skeletal

659   and rounded-embayed shapes of olivine observed in the natural samples

660   (Dayton et al., 2023; Day et al., 2022; Pankhurst et al., 2022) were

661   reproduced in the experiments with up to 1 wt% H_2O added. In general,

662   rounded-embayed crystal shapes found in natural rocks can be ascribed

663   to dissolution processes. However, regarding experimental samples, we

664   want to highlight that embayed olivine crystals can be generated with a

665   small degree of undercooling (25 °C) of the system (Shea et al., 2019).

666   Likely because when the experimental conditions are close to those

667   required for the beginning of crystallisation of a mineral phase, small

668   and unavoidable physical-chemical changes (e.g., temperature, water

669   activity, oxygen fugacity) could generate a series of precipitation-

670   dissolution cycles of unstable skeletal crystals. Following our phase

671   diagram (Fig. 2) it is suggested that with 3 wt% water embayed olivine

672   crystals could appear in the range 1075-1088 °C. This consideration

673 allows us to constrain the pre-eruptive water content of the magma to no

674 more than 3 wt% in presence of the mineralogical assemblage olivine +

675 clinopyroxene + oxide.

676 The estimated pre-eruptive temperatures in the range 1075-

677 1088 °C (3 wt% H_2O) and around 1100 °C (1 wt% H_2O) are comparable

678 with the measured temperatures (1100-1140 °C) of the erupted lavas just

679 outside the vent (Carracedo et al., 2022) as well as with the high pre-

680 eruptive temperatures (1110-1185 °C) estimated for the basanite erupted

681 at El Hierro during 2011-2012 (Martí et al., 2013).

682 Moreover, the thermodynamic simulations performed for the

683 tephritic composition at NNO + 1.5 predict compositional ranges for

684 clinopyroxene (Wo_{39-47}) and olivine (Fo_{79-82}) in good agreement with

685 the natural samples (Wo_{47-50}, Fo_{78-86} (Castro and Feisel, 2022; Day et al.,

686 2022; Pankhurst et al., 2022; Romero et al., 2022)).

687 The absence of plagioclase in the experimental charges and their

688 reproduction in the thermodynamic simulations at lower (<25 MPa)

689 pressures, than the experimental ones, suggest that plagioclase

690 crystallisation was restricted to shallower depths (<1 km) and/or to

691 subaerial conditions during the cooling of the lava flows.

692 Finally, the formation of amphibole at pressures higher than 300

693 MPa obtained with the thermodynamic simulations and its absence in

694 most of the experimental charges seem to suggest that its crystallisation

695 occurred between 20 and 25 km depth (D' Auria et al., 2022; Dayton et

696 al., 2023). In the presence of a H_2O-CO_2 mixed fluid, crystallisation of

697 amphibole may be promoted at lower pressures than 300 MPa, but the

698   absence of amphibole in part of the natural samples or the presence of

699   resorbed amphibole crystals indicate that amphibole was destabilized

700   during magma ascent towards the surface.

701

702   **5. Conclusions**

703

704   The major goal of this research was to constrain the pre-eruptive

705   water and temperature conditions of the magma stored in the shallow

706   2021 Tajogaite eruption reservoir at a depth of 8-12 km beneath Cumbre

707   Vieja volcano by combining experimental phase equilibrium of erupted

708   tephrite with thermodynamic modelling for tephritic and basanitic

709   compositions. Our results suggest that the magma is high temperature

710   (~1100 °C) and relatively water-rich (up to 3 wt%), that it fractionated

711   the assemblage oxide + olivine + clinopyroxene in the shallow reservoir,

712   and that plagioclase microlites crystallised during magma ascent

713   towards the surface (<1 km depth) and/or outside the vent with cooling

714   of erupted products. Further experimental works and thermodynamic

715   simulations involving the presence of a mixed H_2O-CO_2 fluid are

716   needed to reconcile the differences in amphibole crystallisation between

717   the results of our experiments and simulations results and those

718   experimental results reported in literature and to clarify the conditions of

719   amphibole crystallisation during the Tajogaite 2021 eruption. Finally,

720   the results presented in this work contribute to the experimental

721   characterization of tephritic and basanitic magma and have the potential

722   to be applicable to similar magmatic systems in hot-spot zones.

CRediT authorship contribution statement

Alessandro Fabbrizio: Conceptualization, Investigation, Writing – original draft, Writing – review & editing, Funding acquisition. **Emily C. Bamber:** Methodology, Investigation, Writing – original draft, Writing – review & editing. **Eleni Michailidou:** Investigation, Writing – review & editing, Funding acquisition. **Jorge E. Romero:** Conceptualization, Writing – review & editing, Funding acquisition. **Fabio Arzilli**: Conceptualization, Investigation, Writing – original draft, Writing – review & editing, Funding acquisition. **Barbara Bonechi:** Conceptualization, Writing – review & editing, Funding acquisition. **Margherita Polacci:** Conceptualization, Writing – review & editing, Funding acquisition. **Mike Burton:** Conceptualization, Writing – review & editing, Funding acquisition.

Acknowledgments

References

Andújar, J., Costa, F., Martí, J., Wolff, J.A., Carroll, M.R., 2008. Experimental constraints on pre-eruptive conditions of phonolitic magma from the caldera-forming El Abrigo eruption, Tenerife (Canary Islands). Chem. Geol. 257, 173-194. https://doi.org/10.1016/j.chemgeo.2008.08.012.

Andújar, J., Costa, F., Martí, J., 2010. Magma storage conditions of the last eruption of Teide volcano (Canary Islands, Spain). Bull. Volcanol. 72, 381-395. https://doi.org/10.1007/s00445-009-0325-3.

Andújar, J., Costa, F., Scaillet, B., 2013. Storage conditions and eruptive dynamics of central versus flank eruptions in volcanic islands: The case of Tenerife (Canary Islands, Spain). J. Volcanol.

773   Geoth.   Res.   260,   62-79.

774   https://doi.org/10.1016/j.jvolgeores.2013.05.004.

775

776   Andújar, J., Scaillet, B., 2012. Experimental constraints on parameters

777   controlling the difference in the eruptive dynamics of phonolitic

778   magmas: the case of Tenerife (Canary Islands). J. Petrol. 53,

779   1777-1806. https://doi.org/10.1093/petrology/egs033.

780

781   Andújar, J., Scaillet, B., Di Carlo, I., Frascerra, D., Mejías, M.J.,

782   Meletlidis, M., Experimental student group from Orléans-Olot

783   2021-2022 course, Casillas, R., Slodczyk, A., Faranda, C.F.,

784   Núñez-Guerrero, E., Scaillet, S., 2023. Phase equilibria point to

785   cold and shallow depth conditions for magma storage at La

786   Palma   2021   eruption.   Goldschmidt   Conference,

787   https://conf.goldschmidt.info/goldschmidt/2023/meetingapp.cgi/

788   Paper/17945.

789

790   Arzilli, F., Agostini, C., Landi, P., Fortunati, A., Mancini, L., Carroll,

791   M.R., 2015. Plagioclase nucleation and growth kinetics in a

792   hydrous basaltic melt by decompression experiments. Contrib.

793   Mineral. Petrol. 170, 55. https://doi.org/10.1007/s00410-015-

794   1205-9.

795

796   Baker, D.R., Eggler, D.H., 1987. Compositions of anhydrous and

797   hydrous melts coexisting with plagioclase, augite, and olivine or

798   low-Ca pyroxene from 1 atm to 8 kbar − Application to the

799   Aleutian volcanic center of Atka. Am. Mineral. 72, 12-28.

800

801   Bali, E., Hartley, M.E., Halldorsson, S.A., Gudfinnsson, G.H.,

802   Jakobsson, S., 2018. Melt inclusion constraints on volatile

803   systematics and degassing history of the 2014-2015 Holuhraun

804   eruption, Iceland. Contrib Mineral. Petrol. 173, 9.

805   https://doi.org/10.1007/s00410-017-1434-1.

806

807   Blundy, J., Cashman, K., 2008. Petrologic reconstruction of magmatic

808   system variables and processes, in: Putirka, K.D., Tepley III, F.J.

809   (Eds.), Minerals, Inclusions and Volcanic Processes. Rev.

810   Mineral. 69, 179-239. https://doi.org/10.2138/rmg.2008.69.6.

811

812   Bonadonna, C., Pistolesi, M., Biass, S., Voloschina, M., Romero, J.,

813   Coppola, D., Folch, A., D'Auria, L., Martin-Lorenzo, A.,

814   Dominguez, L., Pastore, C., Hardy, M.P.R., Rodriguez, F., 2022.

815   Physical characterization of long-lasting hybrid eruptions: the

816   2021 Tajogaite eruption of Cumbre Vieja (La Palma, Canary

817   Islands). J. Geophys. Res. Solid 127.

818   https://doi.org/10.1029/2022JB025302.

819

820   Carracedo, J.C., Troll, V.R., Day, J.M.D., Geiger, H., Aulinas, M., Soler,

821   V., Deegan, F.M., Perez-Torrado, F.J., Gisbert, G., Gazel, E.,

822   Rodriguez-Gonzalez, A., Albert, H., 2022. The 2021 eruption of

823   the Cumbre Vieja volcanic ridge on La Palma, Canary Islands.

824   Geol. Today 38, 82-120. https://doi.org/10.1111/gto.12388.

825

826 Caracciolo, A., Kahl, M., Bali, E., Gudfinnsson, G.H., Halldorsson, S.A.,

827   Hartley, M.E., 2021. Timescales of crystal mush mobilization in

828   the Baroarbunga-Veioivotn volcanic system based on olivine

829   diffusion chronometry. Am. Mineral. 106, 1083-1096.

830   https://doi.org/10.2138/am-2021-7670.

831

832 Cas, R.A.F., Wolff, J.A., Martí, J., Olin, P.H., Edgar, C.J., Pittari, A.,

833   Simmons, J.M., 2022. Tenerife, a complex end member of

834   basaltic oceanic island volcanoes, with explosive polygenetic

835   phonolitic calderas, and phonolitic-basaltic stratovolcanoes.

836   Earth-Sci. Rev. 230, 103990.

837   https://doi.org/10.1016/j.earscirev.2022.103990.

838

839 Castro, J.M., Feisel, Y., 2022. Eruption of ultralow-viscosity basanite

840   magma at Cumbre Vieja, La Palma, Canary Islands. Nat.

841   Commun. 13, 3174. https://doi.org/10.1038/s41467-022030905-

842   4.

843

844 Colle, F., Masotta, M., Costa, S., Mollo, S., Landi, P., Pontesilli, A.,

845   Peres, S., Mancini, L., 2023. Effect of undercooling on
846   clinopyroxene crystallization in a high K basalt: Implications for
847   magma dynamics at Stromboli volcano. Lithos (in press),
848   107327. https://doi.org/10.1016/j.lithos.2023.107327.

849

850 D'Auria, L., Koulakov, I., Prudencio, J., Cabrera-Pérez, I., Ibáñez, J.M.,
851   Barrancos, J., García-Hernández, R., Martínez van Dorth, D.,
852   Padilla, G.D., Przeor, M., Ortega, V., Hernández, P., Peréz, N.M.,
853   2022. Rapid magma ascent beneath La Palma revealed by
854   seismic tomography. Sci. Rep. 12, 17654.
855   https://doi.org/10.1038/s41598-022-21818-9.

856

857 Day, J.M.D., Troll, V.R., Aulinas, M., Deegan, F.M., Geiger, H.,
858   Carracedo, J.C., Pinto, G.G., Perez-Torrado, F.J., 2022. Mantle
859   source characteristics and magmatic processes during the 2021
860   La Palma eruption. Earth Planet. Sci. Lett. 597, 117793.
861   https://doi.org/10.1016/j.epsl.2022.117793.

862

863 Dayton, K., Gazel, E., Wieser, P., Troll, V.R., Varracedo, J.C., La
864   Madrid, H., Roman, D.C., Ward, J., Aulinas, M., Geiger, H.,
865   Deegan, F.M., Gisbert, G., Perez-Torrado, F.J., 2023. Deep
866   magma storage during the 2021 La Palma eruption. Sci. Adv. 9,
867   eade7641. https://doi.org/10.1126/sciadv.ade7641.

868

869 Di Fiore, F., Vona, A., Scarani, A., Giordano, G., Romano, C., Giordano,

870   D., Caricchi, L., Lorenzo, A.M., Rodriguez, F., Coldwell, B.,

871   Hernandez, P., Pankhurst, M., 2023. Experimental constraints of

872   the rheology of lavas from 2021 Cumbre Vieja eruption (La

873   Palma, Spain). Geophys. Res. Lett. 50, e2022GL100970.

874   https://doi.org/10.1029/2022GL100970.

875

876 Fabbrizio, A., Rouse, P.J., Carroll, M.R., 2006. New experimental data

877   on biotite + magnetite + sanidine saturated phonolitic melts and

878   application to the estimation of magmatic water fugacity. Am.

879   Mineral. 91, 1863-1870. https://doi.org/10.2138/am.2006.2055.

880

881 Fabbrizio, A., Schmidt, M.W., Petrelli, M., 2021. Effect of fO$_2$ on Eu

882   partitioning between clinopyroxene, orthopyroxene and basaltic

883   melt: Development of a Eu^{3+}/Eu^{2+} oxybarometer. Chem. Geol

884   559, 119967. https://doi.org/10.1016/j.chemgeo.2020.119967.

885

886 Faure, F., Trolliard, G., Nicollet, C., Montel, J.M., 2003. A

887   developmental model of olivine morphology as a function of the

888   cooling rate and the degree of undercooling. Contrib. Mineral.

889   Petrol. 145, 251-263. https://doi.org/10.1007/s00410-003-0449-

890   y.

891

892 Faure, F., Schiano, P., Trolliard, G., Nicollet, C., Soulestin, B., 2007.

893   Textural evolution of polyhedral olivine experiencing rapid

894   cooling rates. Contrib. Mineral. Petrol. 153, 405-416.

895   https://doi.org/10.1007/s00410-006-0154-8.

896

897 Freise, M., Holtz, F., Nowak, M., Scoates, J.S., Strauss, H., 2009.

898   Differentiation and crystallization conditions of basalts from the

899   Kerguelen large igneous province: an experimental study.

900   Contrib. Mineral. Petrol. 158, 505-527.

901   https://doi.org/10.1007/s00410-009-0394-5.

902

903 Ghiorso, M.S., Sack, R.O., 1995. Chemical mass-transfer in magmatic

904   processes .4. A revised and internally consistent thermodynamic

905   model for the interpolation and extrapolation of liquid-solid

906   equilibria in magmatic systems at elevated-temperatures and

907   pressures. Contrib. Mineral. Petrol. 119, 197-212.

908   https://doi.org/10.1007/BF00307281.

909

910 Gualda, G.A.R., Ghiorso, M.S., Lemons, R.V., Carley, T.L., 2012.

911   Rhyolite-MELTS: a modified calibration of MELTS optimized

912   for silica-rich, fluid-bearing magmatic systems. J. Petrol. 53,

913   875-890. https://doi.org/10.1093/petrology/egr080.

914

915 Haddadi, B., Sigmarsson, O., Larsen, G., 2017. Magma storage beneath

916   Grimsvotn volcano, Iceland, constrained by clinopyroxene-melt

917   thermobarometry and volatiles in melts inclusions and

918   groundmass glass. J. Geophys. Res. Solid 122, 6984-6997.

919   https://doi.org/10.1002/2017JB014067.

920

921   Hartley, M.E., Bai, E., Maclennan, J., Neave, D.A., Halldorsson, S.A.,

922   2018. Melt inclusion constraints on petrogenesis of the 2014-

923   2015 Holuhraun eruption, Iceland. Contrib. Mineral. Petrol. 173,

924   10. https://doi.org/10.100/s00410-017-1435-0.

925

926   Hildner, E., Klugel, A., Hansteen, T.H., 2012. Barometry of lavas from

927   the 1951eruption of Fogo, Cape Verde Islands: Implications for

928   historic and prehistoric magma plumbing systems. J. Volcanol.

929   Geotherm. Res. 217, 73-90.

930   https://doi.org/10.1016/j.jvolgeores.2011.12.014.

931

932   Houghton, B.F., Gonnermann, H.M., 2008. Basaltic explosive

933   volcanism: Constraints from deposits and models. Geochem. 68,

934   117-140. https://doi.org/10.1016/j.chemer.2008.04.002.

935

936   Hughes, E.C., Buse, B., Kearns, S.L., Blundy, J.D., Kilgour, G., Mader,

937   H.M., 2019. Low analytical totals in EPMA of hydrous silicate

938   glass due to sub-surface charging: Obtaining accurate volatiles

939   by difference. Chem. Geol. 505, 48-56.

940   https://doi.org/10.1016/chem.geo.2018.11.015.

941

942   Iacovino, K., Oppenheimer, C., Scaillet, B., Kyle, P., 2016. Storage and

943   evolution of mafic and intermediate alkaline magmas beneath

944   Ross Island, Antarctica. J. Petrol. 57, 93-118.

945   https://doi.org?10.1093/petrology/egv083.

946

947 Kirkpatrick, J.R., 1981. Kinetics of crystallization of igneous rocks, in:

948   Lasaga, A.C., Kirkpatrick, J.R. (Eds.), Kinetics of Geochemical

949   Processes. Rev. Mineral. Geochem. 8, 321-398.

950

951 Klugel, A., Hansteen, T.H., Galipp, K., 2005. Magma storage and

952   underplating beneath Cumbre Vieja Volcano, La Palma (Canary

953   Islands). Earth Planet. Sci. Lett. 236, 211-226.

954   https://doi.org/10.1016/j.epsl.2005.04.006.

955

956 Kovalenko, V.I., Naumov, V.B., Girnis, A.V., Dorofeeva, V.A.,

957   Yarmolyuk, V.V., 2007. Volatiles in basaltic magmas of ocean

958   islands and their mantle sources: I. Melt compositions deuced

959   from melt inclusions and glasses in the rocks. Geochem. Int. 45,

960   105-122. https://doi.org/10.1134/S0016702907020012.

961

962 Lang, S., Mollo, S., France, L., Misiti, V., Nazzari, M., 2021. Kinetic

963   partitioning of major-minor cations between olivine and

964   Hawaiian tholeiitic basalt under variable undercooling and

965   cooling rate conditions. Chem. Geol. 584, 120485.

966   https://doi.org/10.1016/j.chemgeo.2021.120485.

967

968   La Spina, G., Burton, M., Vitturi, M.D., Arzilli, F., 2016. Role of syn-

969   eruptive plagioclase disequilibrium crystallization in basaltic

970   magma ascent dynamics. Nat. Commun. 7, 13402.

971   https://doi.org/10.1038/ncomms13402.

972

973   Longpré, M.-A., Stix, J., Klügel, A., Shimizu, N., 2017. Mantle to

974   surface degassing of carbon- and sulphur-rich alkaline magma at

975   El Hierro, Canary Islands. Earth Planet. Sci. Lett. 460, 268-280.

976   https://doi.org/10.1016/j.epsl.2016.11.043.

977

978   MacDonald, A., Ubide, T., Mollo, S., Masotta, M., Pontesilli, A., 2022.

979   Trace element partitioning in zoned clinopyroxene as a proxy for

980   undercooling: Experimental constraints from trachybasaltic

981   magmas. Geochim. Cosmochim. Acta 336, 249-268.

982   https://doi.org/10.1016/j.gca.2022.09.007.

983

984   Martí, J., Castro, A., Rodríguez, C., Costa, F., Carrasquilla, S., Pedreira,

985   R., Bolos, X., 2013. Correlation of magma evolution and

986   geophysical monitoring during the 2011-2012 El Hierro (Canary

987   Islands) submarine eruption. J. Petrol. 54, 1349-1373.

988   https://doi.org/10.1093/petrology/egt014.

989

990   Martínez-Martínez, J., Mediato, J.F., Mata, M.P., Ordóñez, B., del

991   Moral, B., Bellido, E., Pérez-López, R., Rodríguez-Pascua, M.A.,

992   Vegas, J., Lozano Otero, G., Mateos, R.M., Sánchez, N.,

993   Galindo, I., 2023. Early fumarolic minerals from the Tajogaite

994   volcanic eruption (La Palma 2021). J. Volcanol. Geotherm. Res.

995   435, 107771. https://doi.org/10.1016/j.jvolgeores.2023.107771.

996

997   Masotta, M., Freda, C., Gaeta, M., 2012. Origin of crystal-poor,

998   differentiated magmas: insights from thermal gradient

999   experiments. Contrib. Mineral. Petrol. 163, 49-65.

1000   https://doi.org/10.1007/s00410-011-0658-8.

1001

1002   Masotta, M., Pontesilli, A., Mollo, S., Armienti, P., Ubide, T., Nazzari,

1003   M., Scarlato, P., 2020. The role of undercooling during

1004   clinopyroxene growth in trachybasaltic magmas: Insights on

1005   magma decompression and cooling at Mt. Etna volcano.

1006   Geochim. Cosmochim. Acta 268, 258-276.

1007   https://doi.org/10.1016/j.gca.2019.10.009.

1008

1009   Moschini, P., Mollo, S., Gaeta, M., Fanara, S., Nazzari, M., Petrone,

1010   C.M., Scarlato, P., 2021. Parameterization of clinopyroxene

1011   growth kinetics via crystal size distribution (CSD) analysis:

1012   Insights into the temporal scales of magma dynamics at Mt. Etna

1013   volcano. Lithos 396, 106225.

1014   https://doi.org/10.1016/j.lithos.2021.106225.

1015

1016   Oglialoro, E., Frezzotti, M.L., Ferrando, S., Tiraboschi, C., Principe, C.,

1017   Groppelli, G.,Villa, I.M., 2017. Lithospheric magma dynamics

1018   beneath the El Hierro Volcano, Canary Islands: insights from

1019   fluid inclusions. Bull. Volcanol. 79, 70.

1020   https://doi.org/10.1007/s00445-017-1152-6.

1021

1022 Padron, E., Perez, N.M., Hernandez, P.A., Sumino, H., Melian, G.V.,

1023   Alonso, M., Rodriguez, F., Asensio-Ramos, M., D'Auria, L.,

1024   2022. Early precursory changes in the He-3/He-4 ratio prior to

1025   the 2021 Tajogaite eruption at Cumbre Vieja Volcano, La Palma,

1026   Canary Islands. Geophys. Res. Lett. 49, e2022GL099992.

1027   https://doi.org/10.1029/2022GL099992.

1028

1029 Pankhurst, M.J., Scarrow, J.H., Barbee, O.A., Hickey, J, Coldwell, B.C.,

1030   Rollinson, G.K., Rodríguez-Losada, J.A., Martín-Lorenzo, A.,

1031   Rodríguez, F., Hernández, W., Calvo Fernández, D., Hernández,

1032   P.A., Pérez, N.M., 2022. Rapid response petrology for the

1033   opening eruptive phase of the 2021 Cumbre Vieja eruption, La

1034   Palma, Canary Islands. Volcanica 5(1), 1-10.

1035   https://doi.org/10.30909/vol.05.01.0110.

1036

1037 PEVOLCA, 2021. Plan Especial de Protección Civil y Atención de

1038   Emergencias por riesgo volcánico en la Comunidad Autónoma

1039   de Canarias. https://info.igme.es/eventos/Erupcion-volcanica-la-

1040   palma/pevolca (accessed 10 July 2023).

1041

1042   Polacci, M., Arzilli, F., La Spina, G., Le Gall, N., Cai, B., Hartley, M.E.,

1043   Di Genova, D., Vo, N.T., Nonni, S., Atwood, R.C., Llewellin,

1044   E.W., Lee, P.D., Burton, M.R., 2018. Crystallisation in basaltic

1045   magmas revealed via in situ 4D synchrotron X-ray

1046   microtomography. Sci. Rep. 8, 8377.

1047   https://doi.org/10.1038/s41598-018-26644-6.

1048

1049   Romero, J.E., Burton, M., Caceres, F., Taddeucci, J., Civico, R., Ricci,

1050   T., Pankhurst, M.J., Hernandez, P.A., Bonadonna, C., Llewellin,

1051   E.W., Pistolesi, M., Polacci, M., Solana, C., D'Auria, L., Arzilli,

1052   F., Andronico, D., Rodriguez, F., Asensio-Ramos, M., Martin-

1053   Lorenzo, A., Hayer, C., Scarlato, P., Perez, N.M., 2022. The

1054   initial phase of the 2021 Cumbre Vieja ridge eruption (Canary

1055   Islands): products and dynamics controlling edifice growth and

1056   collapse. J. Volcanol. Geotherm. Res. 431, 107642.

1057   https://doi.org/10.1016/j.jvolgeores.2022.107642.

1058

1059   Shea, T., Hammer, J.E., Helleband, E., Mourey, A.J., Costa, F., First,

1060   E.C., Lynn, K.J., Melnik, O., 2019. Phosphorus and aluminum

1061   zoning in olivine: contrasting behavior of two nominally

1062   incompatible trace elements. Contrib. Mineral. Petrol. 174, 95.

1063   https://doi.org/10.1007/s00410-019-1639-6.

1064

1065   Taracsák, Z., Hartley, M.E., Burgess, R., Edmonds, M., Iddon, F.,

1066 Longpré, M.-A., 2019. High fluxes of deep volatiles from ocean

1067 island volcanoes: Insights from El Hierro, Canary Islands.

1068 Geochim. Cosmochim. Acta 258, 19-36.

1069 https://doi.org/10.1016/j.gca.2019.05.020.

1070

1071 Ubide, T., Márquez, Á., Ancochea, E., Huertas, M.J., Herrera, R.,

1072 Coello-Bravo, J.J., Sanz-Mangas, D., Mulder, J., MacDonald, A.,

1073 Galindo, I., 2023. Discrete magma injections drive the 2021 La

1074 Palma eruption. Sci. Adv. 9, eadg4813.

1075 https://doi.org/10.1126/sciadv.adg4813.

1076

1077 Walowski, K.J., Kirstein, L.A., De Hoog, J.C.M., Elliott, T.R., Savov,

1078 I.P., Jones, R.E., 2019. Investigating ocean island mantle source

1079 heterogeneity with boron isotopes in melt inclusions. Earth

1080 Planet. Sci. Lett. 508, 97-108.

1081 https://doi.org/10.1016/j.epsl.2018.12.005.

1082

1083 Wang, J., Xiong, X., Takahashi, E., Zhang, L., Li, L., Liu, X., 2019.

1084 Oxidation state of arc mantle revealed by partitioning of V, Sc

1085 and Ti between mantle minerals and basaltic melts. J. Geophys.

1086 Res., Solid Earth 124, 4617-4638.

1087 https://doi.org/10.1029/2018JB016731.

1088

1089 Weis, F.A., Skogby, H., Troll, V.R., Deegan, F.M., Dahren, B., 2015.

1090 Magmatic water contents determined through clinopyroxene:

1091 Examples from the Western Canary Islands, Spain. Geochem.

1092 Geophys. Geosystems 16, 2127-2146.

1093 https://doi.org/10.1002/2015GC005800.

1094

1095 **Figure and Table Captions**

1096

1097 **Fig. 1.** BSE images of selected experimental runs. (a) Crystallisation run

1098 at 1100 °C/1 wt% H_2O: euhedral clinopyroxene (Cpx) with

1099 sectors enriched in Si-Mg (darker sectors) and in Ti-Al (brighter

1100 sectors), skeletal olivine (Ol) with embayements and melt

1101 pockets, and euhedral chromium spinel (Cr-spinel). (b)

1102 Crystallisation run at 1125 °C/1 wt% H_2O: euhedral olivine and

1103 chromium spinel. (c) Reversal experiment at 1100 °C/1 wt%

1104 H_2O with a run duration of 48 hours: euhedral clinopyroxene,

1105 euhedral olivine with melt pocket and olivine with embayements,

1106 euhedral chromium spinel. (d) Reversal experiment with 1 wt%

1107 H_2O added heated directly from room temperature to 1100 °C:

1108 euhedral clinopyroxene with sectors enriched in Si-Mg (darker

1109 sectors) and in Ti-Al (brighter sectors), euhedral olivine and

1110 chromium spinel. The bright zone around the experimental

1111 charges in (a), (b) and (c) is the $Au_{80}Pd_{20}$ capsule. Scale bar

1112 length is 100 μm in all pictures.

1113

1114 **Fig. 2.** Phase diagram showing the stability fields of mineral phases as a

1115   function of experimental temperature and added water. Closed

1116   circles: crystallisation experiments. Arrows: reversal

1117   experiments. Cr-sp: chromium spinel; Ol: olivine; Cpx:

1118   clinopyroxene; Ti-mt: titanium magnetite; Amph: amphibole;

1119   Ap: apatite.

1120

1121   **Fig. 3.** Variations of oxide concentrations (a-l), recalculated to 100 wt%

1122   anhydrous, of the residual melts as a function of experimental

1123   temperature. The black circle shows the bulk-rock composition

1124   of the natural tephrite (CVLP-LF3; Romero et al., 2022). The

1125   dotted horizontal lines shows the minimal and maximal oxide

1126   concentrations in natural glasses (Castro and Feisel 2022;

1127   Romero et al., 2022; Dayton et al., 2023). The vertical dashed

1128   lines show the crystallisation temperature of clinopyroxene

1129   (Cpx) and apatite (Ap). (a) SiO_2; (b) Al_2O_3; (c) CaO; (d) MgO;

1130   (e) FeO; (f) TiO_2; (g) MnO; (h) Na_2O; (i) K_2O; (l) P_2O_5. If not

1131   shown error bars are smaller than symbols.

1132

1133   **Fig. 4.** (a) Compositional variations for olivine (olivine Fo%) and (b)

1134   for clinopyroxene (pyroxene Wo%) as a function of

1135   experimental temperature. The dotted horizontal lines shows the

1136   minimal and maximal amount of forsterite and wollastonite in

1137   natural olivine and clinopyroxene (Castro and Feisel 2022; Day

1138   et al., 2022; Pankhurst et al., 2022; Romero et al., 2022; Dayton

1139   et al., 2023).

1140   **Fig. 5.** Ternary classification diagram for pyroxene showing the

1141   experimental (diamonds) and natural (circles) compositions.

1142

1143   **Fig. 6.** Results of Rhyolite-MELTS simulations (a-h), showing phase

1144   diagrams for the tephritic (CVLP-LF3) melt composition as a

1145   function of H_2O content and fO_2. (a) fO_2 = NNO + 1.5, H_2O = 0

1146   wt%; (b) fO_2 = QFM, H_2O = 0 wt%; (c) fO_2 = NNO + 1.5, H_2O =

1147   1 wt%; (d) fO_2 = QFM, H_2O = 1 wt%; (e) fO_2 = NNO + 1.5, H_2O

1148   = 3 wt%; (f) fO_2 = QFM, H_2O = 3 wt%; (g) fO_2 = NNO + 1.5,

1149 H_2O = 5 wt%; (h) fO_2 = QFM, H_2O = 5 wt%. Cpx:

1150   clinopyroxene; Ol: olivine; Plg: plagioclase; Hbl: Hornblende.

1151

1152   **Fig. 7.** Results of Rhyolite-MELTS simulations (a-h), showing phase

1153   diagrams for the basanite melt composition as a function of H_2O

1154   content and fO_2. (a) fO_2 = NNO + 1.5, H_2O = 0 wt%; (b) fO_2 =

1155   QFM, H_2O = 0 wt%; (c) fO_2 = NNO + 1.5, H_2O = 1 wt%; (d) fO_2

1156   = QFM, H_2O = 1 wt%; (e) fO_2 = NNO + 1.5, H_2O = 3 wt%; (f)

1157 fO_2 = QFM, H_2O = 3 wt%; (g) fO_2 = NNO + 1.5, H_2O = 5 wt%;

1158   (h) fO_2 = QFM, H_2O = 5 wt%. Cpx: clinopyroxene; Ol: olivine;

1159   Plg: plagioclase; Hbl: Hornblende.

1160

1161   **Table 1** Starting material compositions.

1162

1163   **Table 2** Experimental conditions at 275 MPa and phase assemblage.

1164

1165 **Supplementary Table 1** EMPA analyses for the synthesized phases and

1166 BSE images of the experimental charges.

1167

1168 **Supplementary Fig. 1** Results of Rhyolite-MELTS simulations (a-h),

1169 considering spinel crystallisation, showing phase diagrams for

1170 the tephritic (CVLP-LF3) melt composition as a function of H_2O

1171 content and fO_2. (a) fO_2 = NNO + 1.5, H_2O = 0 wt%; (b) fO_2 =

1172 QFM, H_2O = 0 wt%; (c) fO_2 = NNO + 1.5, H_2O = 1 wt%; (d) fO_2

1173 = QFM, H_2O = 1 wt%; (e) fO_2 = NNO + 1.5, H_2O = 3 wt%; (f)

1174 fO_2 = QFM, H_2O = 3 wt%; (g) fO_2 = NNO + 1.5, H_2O = 5 wt%;

1175 (h) fO_2 = QFM, H_2O = 5 wt%.

1176

1177 **Supplementary Fig. 2** Results of Rhyolite-MELTS simulations (a-h),

1178 considering spinel crystallisation, showing phase diagrams for

1179 the basanite melt composition as a function of H_2O content and

1180 fO_2. (a) fO_2 = NNO + 1.5, H_2O = 0 wt%; (b) fO_2 = QFM, H_2O =

1181 0 wt%; (c) fO_2 = NNO + 1.5, H_2O = 1 wt%; (d) fO_2 = QFM, H_2O

1182 = 1 wt%; (e) fO_2 = NNO + 1.5, H_2O = 3 wt%; (f) fO_2 = QFM,

1183 H_2O = 3 wt%; (g) fO_2 = NNO + 1.5, H_2O = 5 wt%; (h) fO_2 =
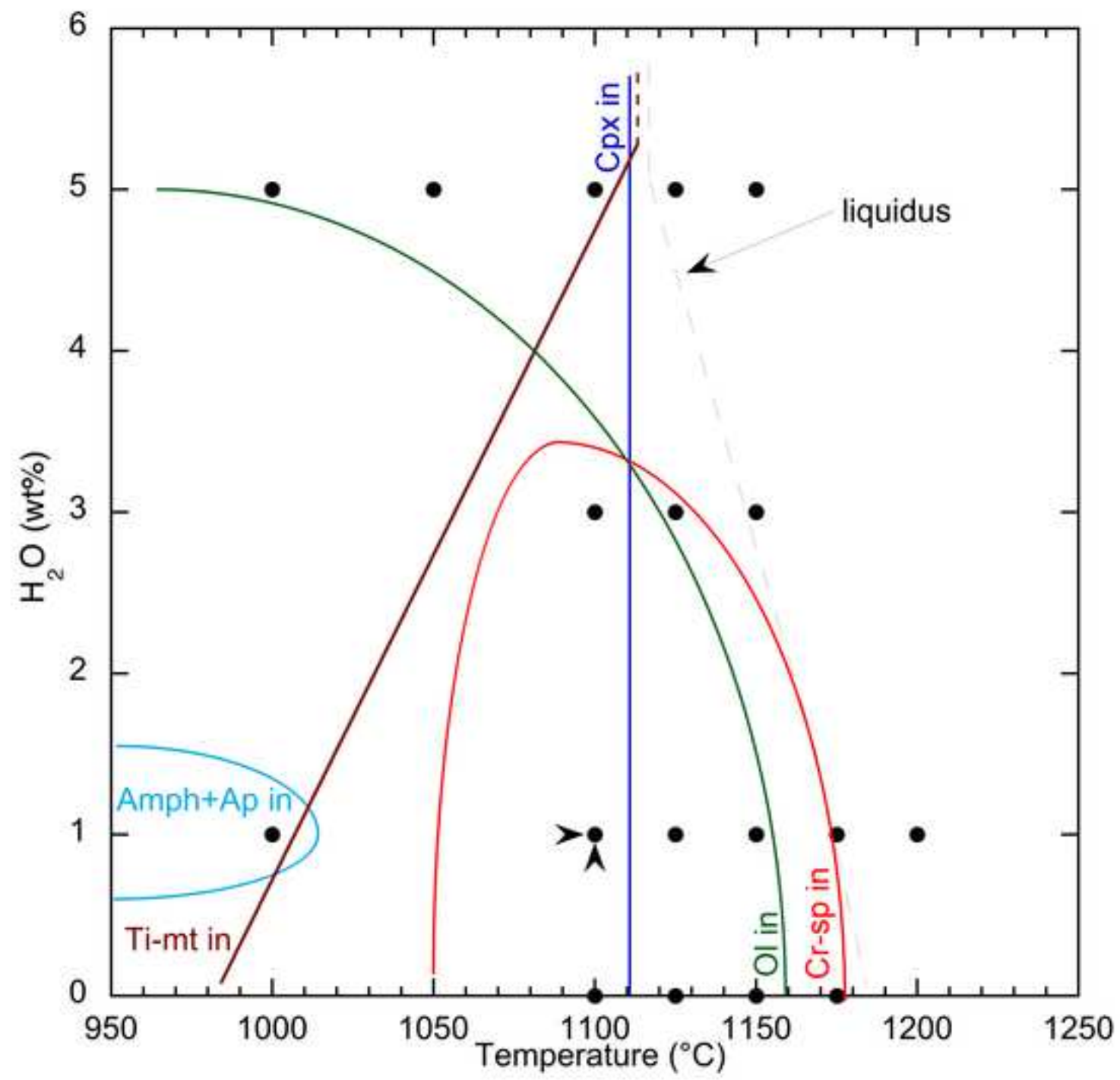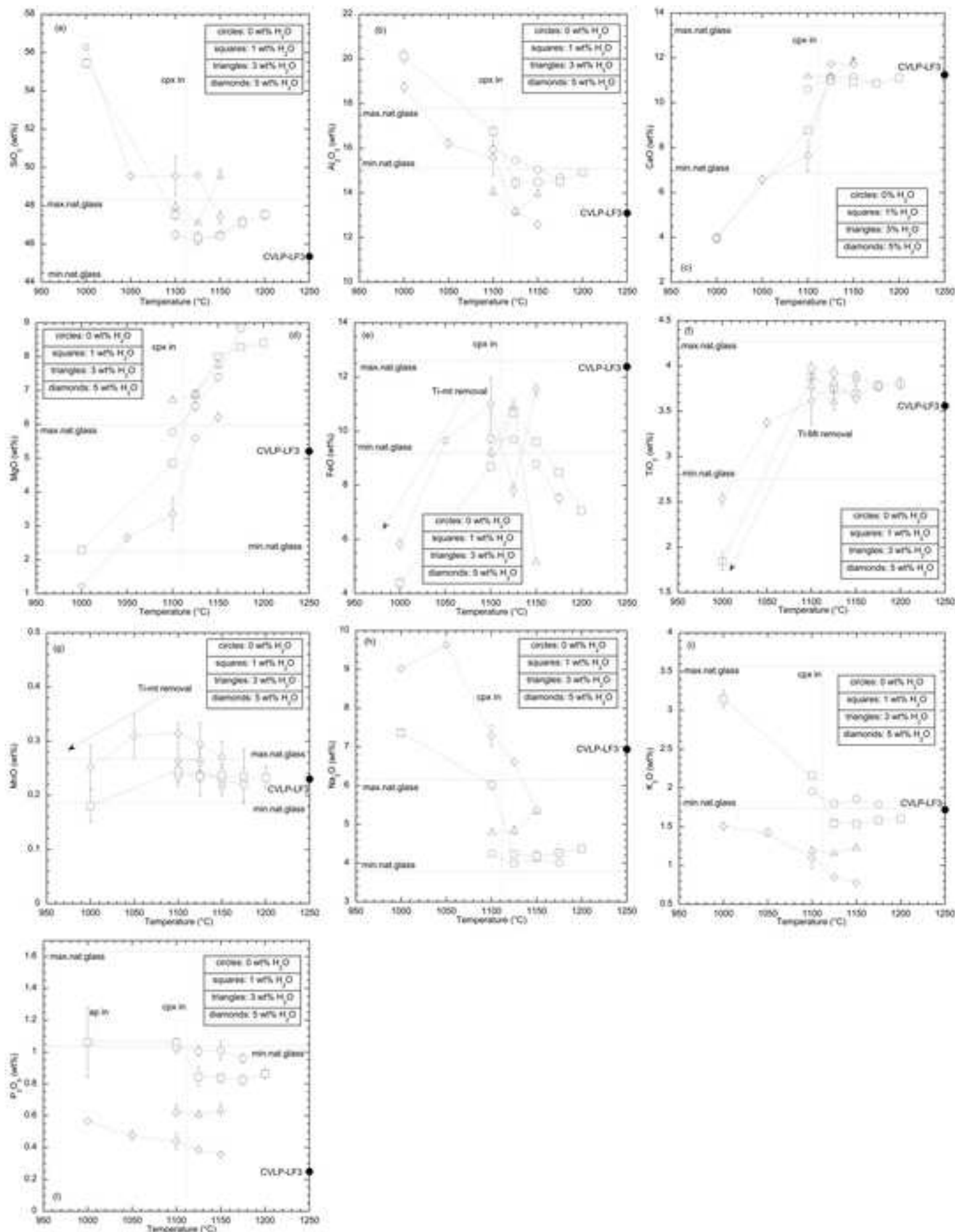
1184 QFM, H_2O = 5 wt%.

1185

1186 **Supplementary Fig. 3** Modelled melt compositions for the tephritic

1187 starting composition CVLP-LF3 at a pressure of 275 MPa and
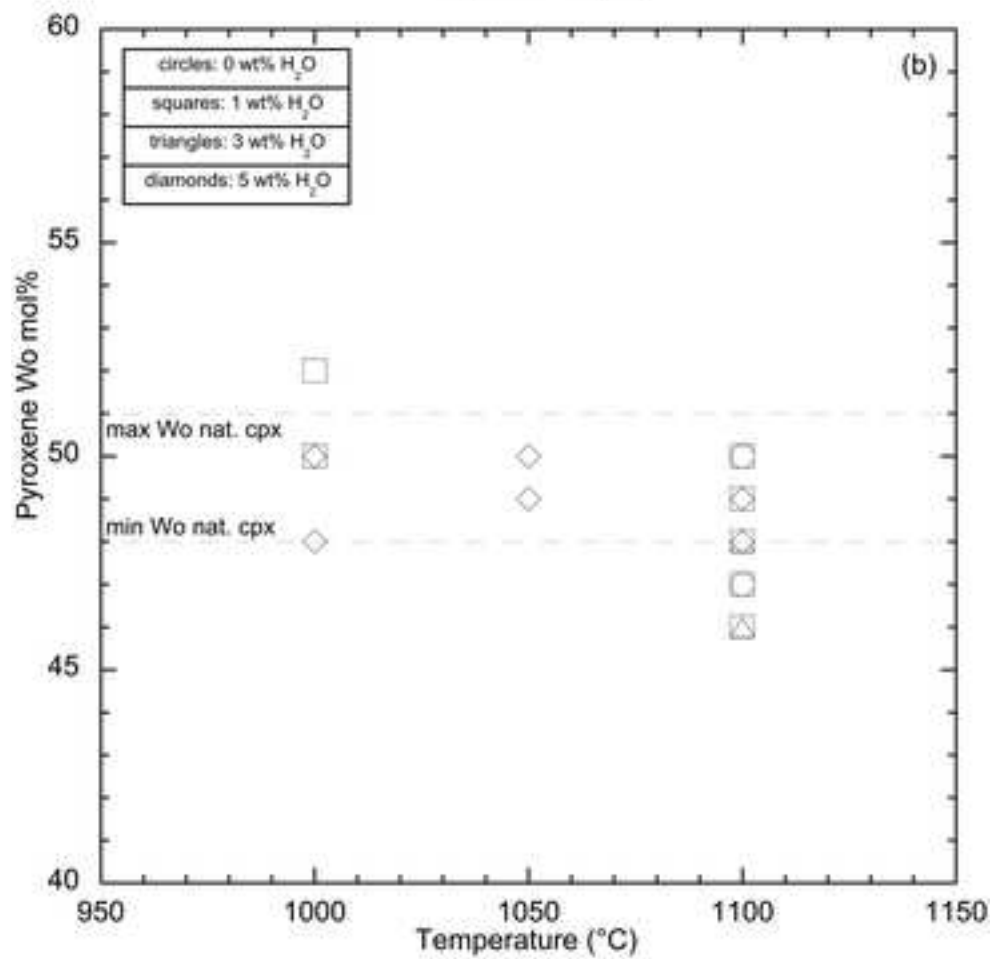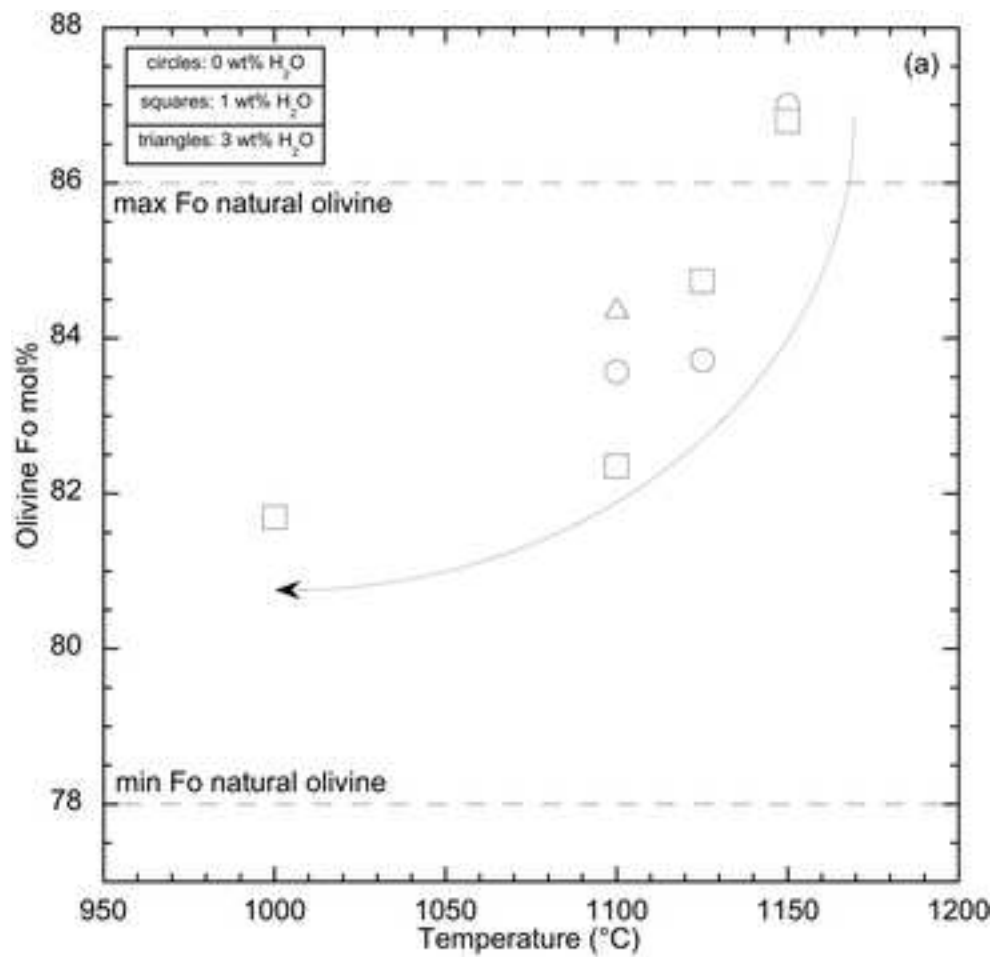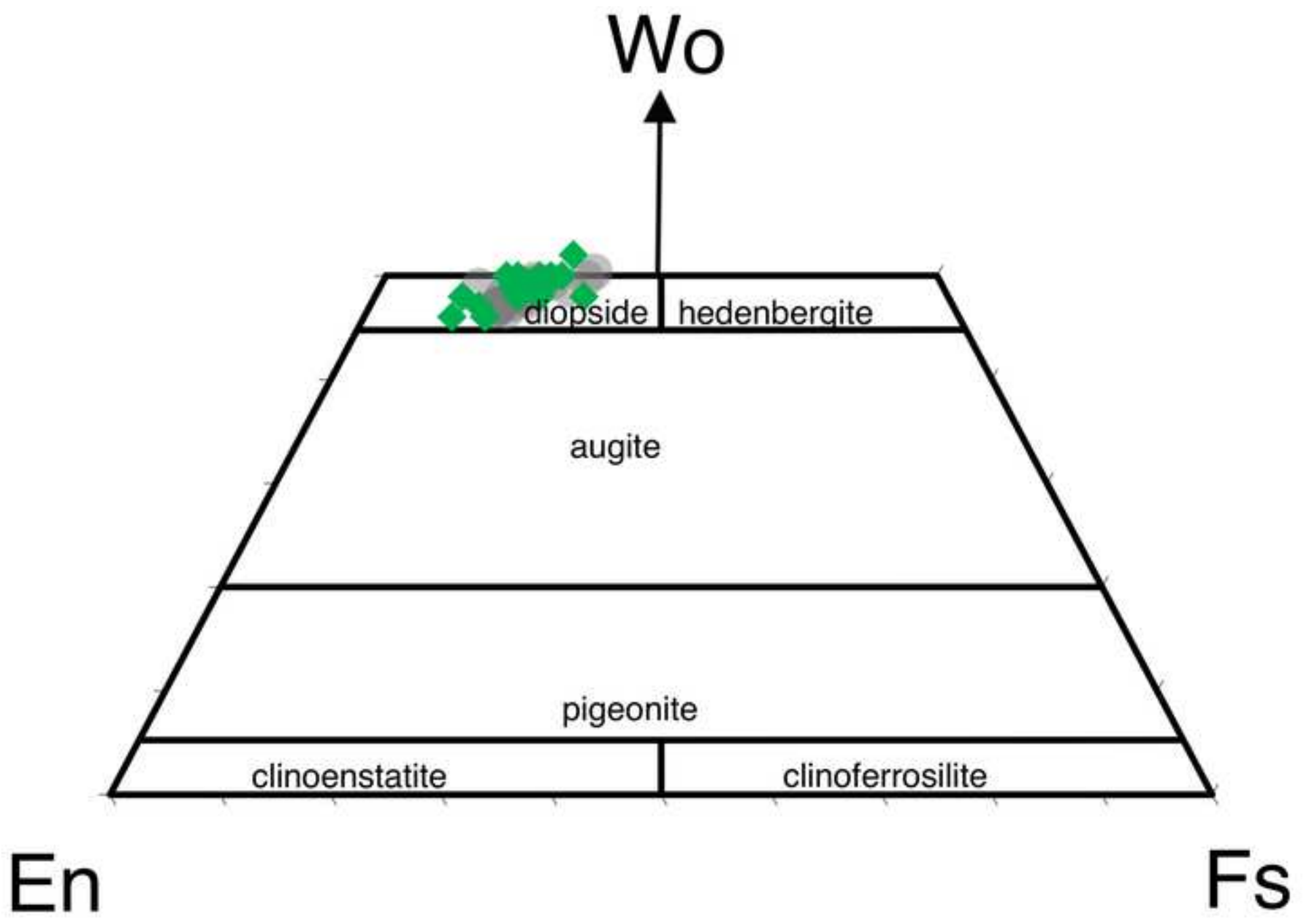
1188 fO_2 = NNO+1.5.

1189

1190   **Supplementary Fig. 4** Modelled melt compositions for the basanitic

1191   composition at a pressure of 275 MPa and $f\text{O}_2$ = NNO+1.5.
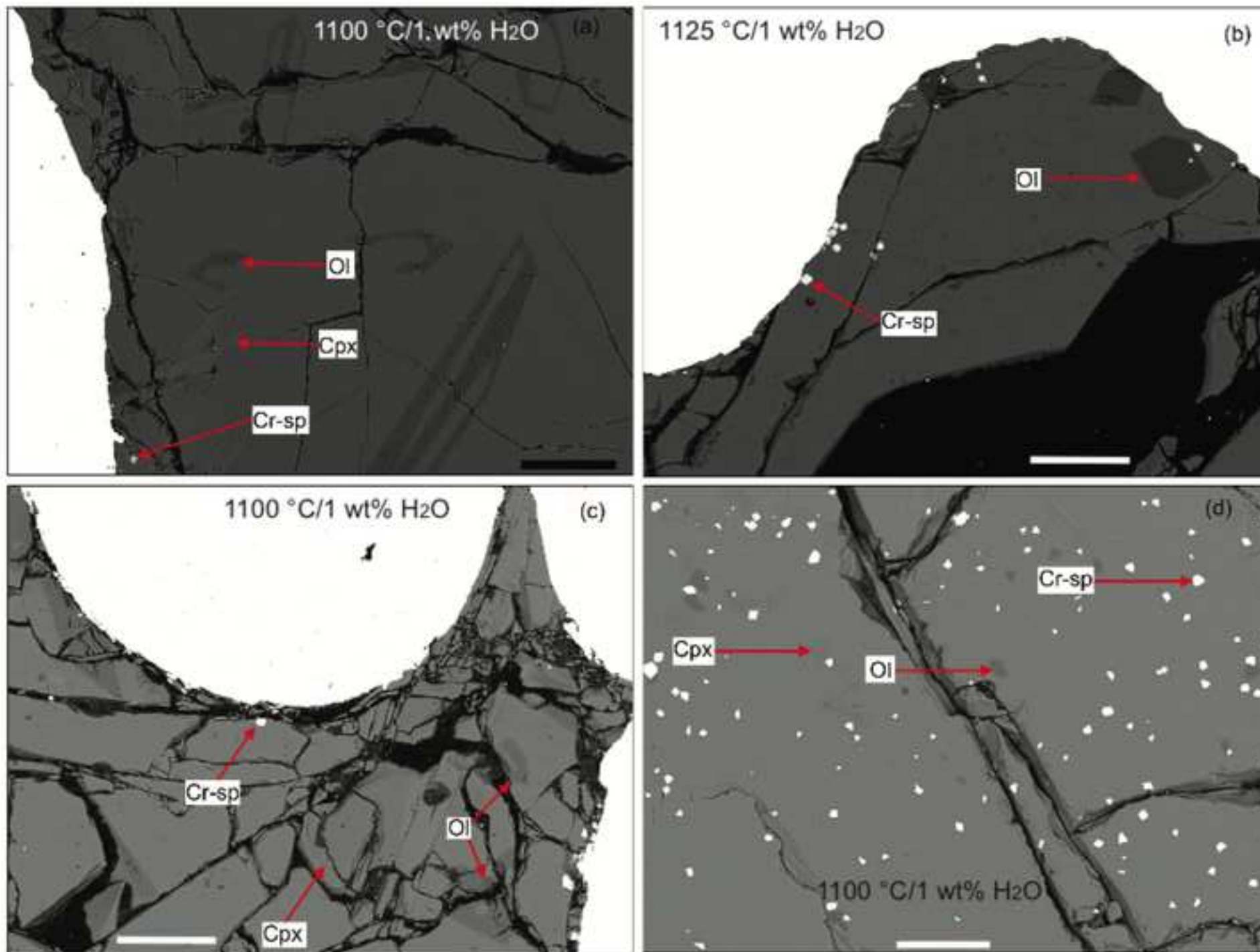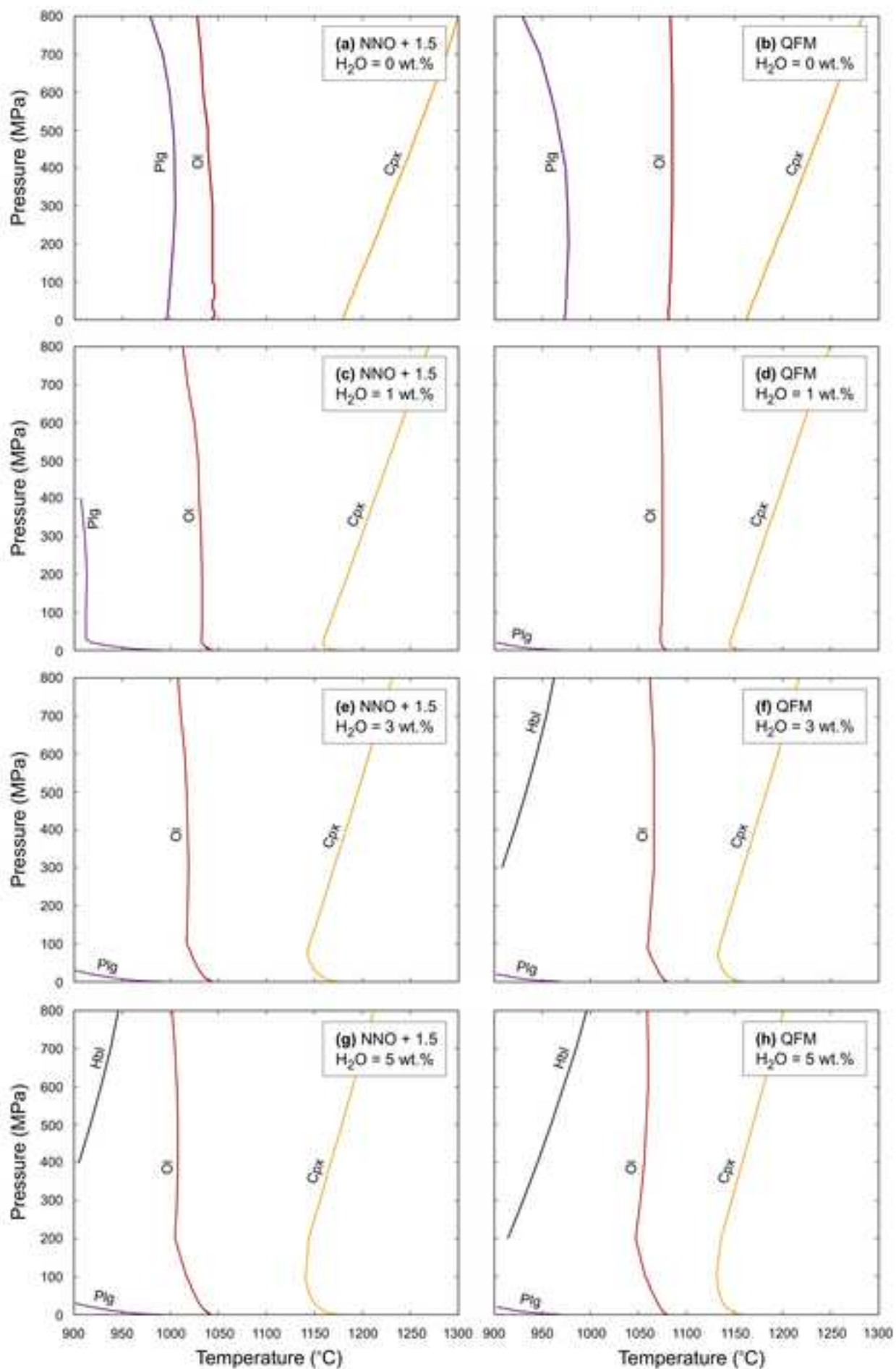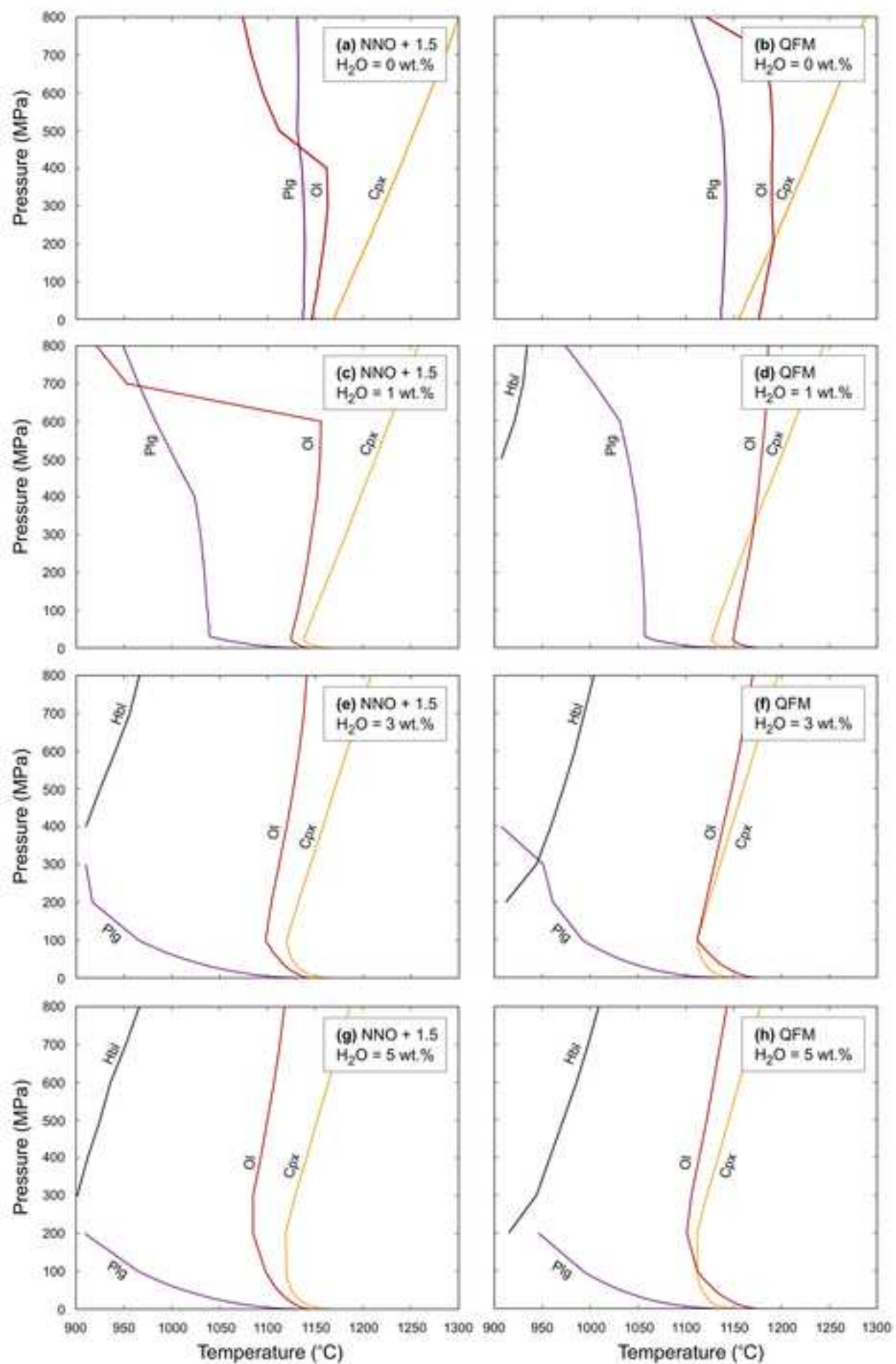
Table 1
Starting material compositions.

	CVLP-LF3	CVLP-LF3-5%	CVLP-LF3-3%	CVLP-LF3-1%
SiO_2 (wt%)	44.90	42.75	43.61	44.47
TiO_2	3.51	3.36	3.42	3.48
Al_2O_3	12.98	12.37	12.61	12.86
FeO	12.26	11.67	11.90	12.14
MnO	0.23	0.24	0.24	0.23
MgO	5.16	4.91	5.01	5.11
CaO	11.15	10.60	10.82	11.04
Na_2O	6.87	6.54	6.67	6.80
K_2O	1.71	1.62	1.66	1.69
P_2O_5	0.25	0.24	0.24	0.25
H_2O[a]	-	4.71	2.83	0.94
TrE[b]	0.99	0.99	0.99	0.99
Total	100.00	100.00	100.00	100.00

The composition of CVLP-LF3 is the natural lava composition (Romero et al. 2022) recalculated to 100% after the addition of 1 wt% trace elements.

The CVLP-LF3-5% composition is the hydrous-rich synthetic composition, analogue to the natural CVLP-LF3, recalculated to 100% after the addition of 5 wt% water and of 1 wt% trace elements.

The CVLP-LF-3% and CVLP-LF3-1% compositions were obtained by mixing the CVLP-LF3 and CVLP-LF3-5% compositions in the ratio 40:60 and 80:20, respectively.

[a]H_2O added as $Al(OH)_3$, see text.
[b]TrE: trace elements